



Denoise diffusion-weighted images using higher-order singular value decomposition

Xinyuan Zhang^{a,1}, Jie Peng^a, Man Xu^a, Wei Yang^a, Zhe Zhang^b, Hua Guo^b, Wufan Chen^a, Qianjin Feng^{a,*}, Ed X. Wu^{a,c,d,*}, Yanqiu Feng^{a,1}

^a School of Biomedical Engineering, Guangdong Provincial Key Laboratory of Medical Image Processing, Southern Medical University, Guangzhou, China

^b Department of Biomedical Engineering, Center for Biomedical Imaging Research, Tsinghua University, Beijing, Beijing, China

^c Laboratory of Biomedical Imaging and Signal Processing, University of Hong Kong, Hong Kong SAR, China

^d Department of Electrical and Electronic Engineering, University of Hong Kong, Hong Kong SAR, China

ARTICLE INFO

Keywords:

Diffusion-weighted imaging (DWI)
Magnetic resonance imaging (MRI)
Diffusion tensor imaging (DTI)
Denoising
Higher-order singular value decomposition (HOSVD)

ABSTRACT

Noise usually affects the reliability of quantitative analysis in diffusion-weighted (DW) magnetic resonance imaging (MRI), especially at high b-values and/or high spatial resolution. Higher-order singular value decomposition (HOSVD) has recently emerged as a simple, effective, and adaptive transform to exploit sparseness within multidimensional data. In particular, the patch-based HOSVD denoising has demonstrated superb performance when applied to T1-, T2-, and proton density-weighted MRI data. In this study, we aim to investigate the feasibility of denoising DW data using the HOSVD transform. With the low signal-to-noise ratio in typical DW data, the patch-based HOSVD denoising suffers from stripe artifacts in homogeneous regions because of the HOSVD bases learned from the noisy patches. To address this problem, we propose a novel denoising method. It first introduces a global HOSVD-based denoising as a prefiltering stage to guide the subsequent patch-based HOSVD denoising stage. The HOSVD bases from the patch groups in prefiltered images are then used to transform the noisy patch groups in original DW data. Experiments were performed using simulated and in vivo DW data. Results show that the proposed method significantly reduces stripe artifacts compared with conventional patch-based HOSVD denoising methods, and outperforms two state-of-the-art denoising methods in terms of denoising quality and diffusion parameters estimation.

Introduction

Diffusion-weighted (DW) magnetic resonance imaging (MRI) provides a non-invasive technique to map the molecular diffusion of in vivo biological tissues. The random molecular Brownian motion in tissues is restricted by structures such as cell membranes, myelin sheaths, macromolecules, etc (Feng et al., 2014). Thus, the diffusion anisotropy information extracted from multidirectional DW images reflects the microscopic characteristic of tissue structures. Quantitative maps and fiber tracking from DW magnetic resonance (MR) data are widely used in the clinical diagnosis of patients with acute ischemic stroke (Kloska et al., 2010; Sotak, 2002), multiple sclerosis (Tievsky et al., 1999; Werring et al., 1999), epilepsy (Eriksson et al., 2001; Hugg et al., 1999) and brain tumors (Bode et al., 2006; Krabbe et al., 1997), as well as in the scientific research of brain anatomical connectivity (Jones et al., 1999; Poupon et al., 2001).

The quantitative analysis of DW data is usually challenged by noise

(Bastin et al., 1998; Kristoffersen, 2012), especially in high-spatial-resolution and/or high-b-value diffusion imaging where signal-to-noise ratio (SNR) is usually low. In regions where white matter fiber bundles intersect or split, high-spatial-resolution DW imaging is required for the accurate estimation of the orientation of fiber bundles (Uğurbil et al., 2013). However, the reduced voxel size in high-spatial-resolution DW imaging will decrease SNR and challenge the quantification of diffusion-related parameters. In addition, to model the non-Gaussian diffusion characteristics in biological tissues, high-b-value DW images are usually acquired in multiple-b-value diffusion MRI (Grinberg et al., 2011; Shimoto et al., 2009). Because the signal magnitude decreases rapidly with b values, the low SNR in high-b-value DW images will degrade the accuracy and reliability of the subsequent quantitative analysis (Jones and Basser, 2004; Wu and Cheung, 2010).

The SNR can be improved by averaging repeated acquisitions at the expense of prolonging scan time and increasing the susceptibility to subject motion. Alternatively, the noise in the DW images and its effect

* Correspondence authors.

E-mail addresses: qianjinfeng08@gmail.com (Q. Feng), ewu@eee.hku.hk (E.X. Wu).

¹ equally contributed

on parameter quantification can be reduced by post-processing techniques that do not increase acquisition time. A number of filtering methods in image processing domain have been applied to denoise DW images, and these methods can be mainly classified into two categories. One category is to impose parameter smoothing constraint during quantification (Liu et al., 2013; Tschumperlé and Deriche, 2003; Wang et al., 2003, 2004) or to filter quantified parameter maps (Castaño-Moraga et al., 2007; Hamarneh and Hradsky, 2007). The other category is to first denoise DW images and then estimate diffusion parameters. The latter approach avoids the bias introduced by diffusion models, and can be integrated with various models for the subsequent analysis. Thus, the latter approach has been widely adopted to reduce the effect of noise on the diffusion parameter mapping in the past few decades. The current DW image denoising methods include algorithms based on wavelet transforms (Wiestam et al., 2006), partial differential equations (Ding et al., 2005; Parker et al., 2000), propagation-separation approaches (Becker et al., 2014, 2012), nonlocal means (Descoteaux et al., 2008; Wiest-Daessle et al., 2007), principal component analysis (Arfanakis et al., 2002; Bao et al., 2013; Manjon et al., 2013), low-rank approximations (Lam et al., 2014, 2016), and sparseness among grouped similar patches (Bao et al., 2013).

Recently, we developed an MR image denoising algorithm based on the higher-order singular value decomposition (HOSVD) transform (Zhang et al., 2015a), which exhibits state-of-the-art performance in denoising T1-, T2- and proton density-weighted MR images. The HOSVD denoising algorithm first groups similar small local cubes (3D patches) into a 4D tensor, then performs the HOSVD transform of the tensor, thresholds the transformed coefficients, and performs the invert HOSVD transform, and finally aggregates multiple estimates of each pixel by a weighted average. The HOSVD transform offers a simple, adaptive and natural way to exploit sparsity along all dimensions of multidimensional data. Compared with conventional MR images, DW images not only contain redundant information across the spatial domain but are also highly correlated along different diffusion directions. The sparse representation of multidimensional structures in DW images can be effectively exploited for noise reduction by using the HOSVD transform.

In this paper, we aim to investigate the application of the HOSVD transform to denoising DW images. In the case of low SNR, we found by experiment that the patch-based HOSVD algorithm introduced stripe-like artifacts in the homogeneous regions of the denoised image. Similar phenomenon was also observed in previous studies on transform-based image denoising (Knaus and Zwicker, 2013, 2014; Pierazzo et al., 2014). We showed by experiment that these artifacts are caused by the noise-deteriorated HOSVD bases learned from the patches with severe noise. To mitigate the artifacts, an intuitive approach is to transform the grouped noisy patches using the HOSVD bases learned from the corresponding noise-free or noise-less patches. Thus, we introduce a global HOSVD prefiltering stage to guide the patch-based local HOSVD method for the improved denoising of DW images. The proposed algorithm is referred as GL-HOSVD for brevity, and is detailed in the Methods section. The performance of GL-HOSVD was evaluated on simulation as well as in vivo DW data contaminated by the spatially-invariant Rician or noncentral Chi noise.

Methods

The HOSVD-based denoising strategy

The HOSVD is a multilinear generalization of the matrix SVD to high-order tensors, and it can achieve the sparse representation of a tensor with adaptive bases (De Lathauwer et al., 2000; Kolda and Bader, 2009). Similar to other transform-based denoising methods, HOSVD-based denoising consists of three main steps. First, the HOSVD transform of the noisy tensor is performed. Then, the transformed coefficients are manipulated by thresholding based on

the assumption that small transform coefficients mainly correspond to noise. Finally, the HOSVD transform is inverted. These steps are detailed as follows.

The multidimensional image corrupted by the additive Gaussian noise can be modeled as:

$$\mathbf{Y} = \mathbf{A} + \mathbf{N} \quad (1)$$

where \mathbf{Y} is a N -order tensor of size $(I_1 \times I_2 \times \dots \times I_N)$ representing the noisy observation, \mathbf{A} a tensor representing the noise-free image, and \mathbf{N} a tensor denoting the zero mean Gaussian noise with a standard deviation (SD) of σ . The denoising algorithm aims to recover an estimate of \mathbf{A} from the noisy observation \mathbf{Y} .

The HOSVD of \mathbf{Y} is given by De Lathauwer et al. (2000):

$$\mathbf{Y} = \mathbf{S} \times_1 \mathbf{U}^{(1)} \times_2 \mathbf{U}^{(2)} \dots \times_N \mathbf{U}^{(N)} \quad (2)$$

where \mathbf{S} is an all-orthogonal and ordered $(I_1 \times I_2 \times \dots \times I_N)$ -tensor that consists of the transform coefficients, $\mathbf{U}^{(n)} \in \mathbb{R}^{I_n \times I_n}$, $n = 1, 2, \dots, N$ an orthogonal unitary matrix, and \times_n a n -mode product of a tensor by a matrix $\mathbf{U}^{(n)}$. Generally, $\mathbf{U}^{(n)}$ is obtained by the SVD of $\mathbf{Y}^{(n)} \in \mathbb{R}^{I_n \times (I_{n+1} \times I_{n+2} \dots \times I_N)}$, which is the n -mode unfolding matrix of the tensor \mathbf{Y} . After that, \mathbf{S} is calculated by projecting \mathbf{Y} onto $\mathbf{U}^{(n)}$, $n = 1, 2, \dots, N$ (De Lathauwer et al., 2000).

The small transform coefficients in tensor \mathbf{S} mainly reflect the contributions from noise. Thus, noise suppression can be achieved by a hard thresholding operation (Rajwade et al., 2013). This operation nullifies the coefficients in \mathbf{S} below a fixed threshold, and is formulated as follows:

$$H_\tau(\mathbf{S}) = \begin{cases} s_{i_1 i_2 \dots i_N} & \text{if } \text{abs}(s_{i_1 i_2 \dots i_N}) \geq \tau \\ 0 & \text{if } \text{abs}(s_{i_1 i_2 \dots i_N}) < \tau \end{cases} \quad (3)$$

where H_τ represents the hard thresholding operator with a threshold τ , and $s_{i_1 i_2 \dots i_N}$ the element of the tensor \mathbf{S} at position (i_1, i_2, \dots, i_N) . The denoising performance highly depends on the threshold. According to Donoho and Johnstone (1994), the threshold τ can be set to $\sigma\sqrt{2 \log(I_1 \times I_2 \times \dots \times I_N)}$, which is an optimal threshold from a statistical risk viewpoint.

Let $\hat{\mathbf{S}}$ denote the coefficient tensor after thresholding, i.e., $\hat{\mathbf{S}} = H_\tau(\mathbf{S})$. An estimate of \mathbf{A} can be obtained by the inverse HOSVD with the bases $\mathbf{U}^{(n)}$, $n = 1, 2, \dots, N$ as follows:

$$\hat{\mathbf{A}} = \hat{\mathbf{S}} \times_1 \mathbf{U}^{(1)} \times_2 \mathbf{U}^{(2)} \dots \times_N \mathbf{U}^{(N)} \quad (4)$$

where $\hat{\mathbf{A}}$ denotes an estimate of the noise-free tensor \mathbf{A} .

Compared with transforms that use fixed bases such as discrete cosine and wavelet, the HOSVD bases $\mathbf{U}^{(n)}$, $n = 1, 2, \dots, N$ are learned from the multidimensional data and thus more adaptive to the structures in data. This adaptive nature enables the HOSVD to be a good sparsifying transform for image restoration and reconstruction (Maggioni et al., 2013; Yu et al., 2014; Zhang et al., 2015a).

The proposed GL-HOSVD algorithm

Motivation for the GL-HOSVD algorithm

The existing HOSVD-based image denoising algorithms can be categorized into two classes. One class is the global HOSVD denoising which considers the whole image series as a single tensor (Letexier and Bourennane, 2008), and the other is the patch-based HOSVD denoising which exploits the sparsity inside the grouped similar patches (Rajwade et al., 2013; Zhang et al., 2015a). In contrast to the global HOSVD (G-HOSVD), we will refer to the patch-based HOSVD as local HOSVD (L-HOSVD). The L-HOSVD method can achieve an effective sparse representation of grouped similar patches, and demonstrates a state-of-the-art performance in denoising natural color images (Rajwade et al., 2013) and conventional MRI volume data (Zhang et al., 2015a). However, the L-HOSVD method is prone to visible artifacts in homogeneous region when SNR is low, similar to other transform-based denoising methods such as BM3D (Dabov et al., 2007; Pierazzo et al., 2014).

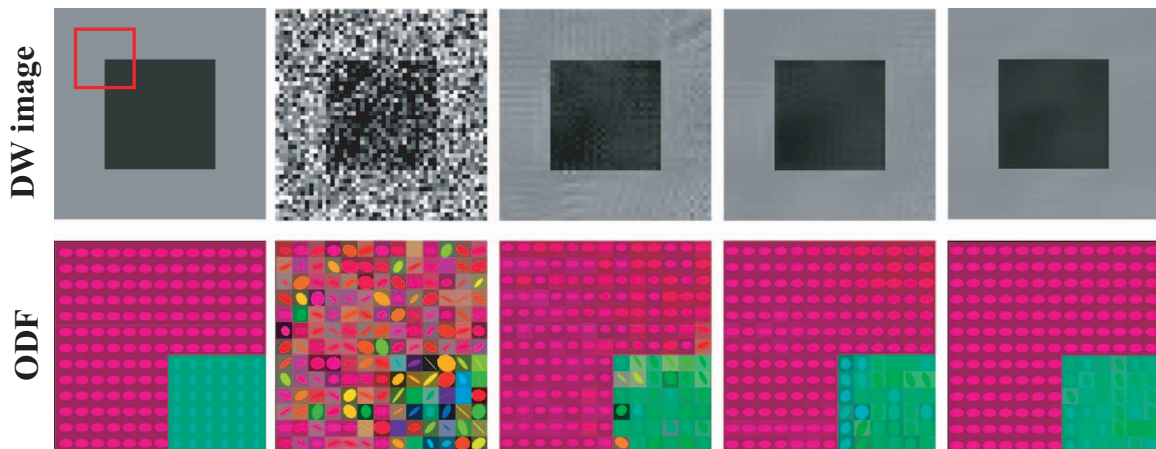


Fig. 1. Denoising results by L-HOSVD using HOSVD bases learned from images under varying noise levels. Top row, from left to right: the noise-free DW image at $b=1500 \text{ s/mm}^2$ along a representative direction, the noisy image with 5% Gaussian noise, and denoising images by L-HOSVD using the HOSVD bases learned from images with 5%, 3% and zero Gaussian noise, respectively. Second row: the corresponding reconstructed ODFs in the red box.

We hypothesize that the artifacts in homogeneous regions are caused by degraded HOSVD bases learned from noisy patches. To justify the hypothesis, we performed experiment using simulated DTI data which consist of two homogeneous regions. The ground-truth DTI data were synthesized using the formula $S_0 \exp(-bg^T \mathbf{D}g)$, where S_0 is the non-diffusion signal, b the b -value in diffusion MRI, \mathbf{g} a unit gradient vector, and \mathbf{D} the diffusion tensor. The tensors of $[3.3, 0, 1.2; 0, 1.8, 0; 1.2, 0, 1.3] \times 10^{-3} \text{ mm}^2/\text{s}$ and $[3, 0, 0; 0, 3.8, -1; 0, -1, 3] \times 10^{-3} \text{ mm}^2/\text{s}$ were separately used for the two regions. For both regions, we set $S_0=1$, $b=1500 \text{ s/mm}^2$ and \mathbf{g} to be 22 uniformly-spaced directions in terms of spherical coordinates. The above synthesized data was added with Gaussian noise of varying levels, which was expressed as a percentage and defined as the ratio of the SD of the noise to S_0 .

The top row in Fig. 1 shows the denoising results of L-HOSVD on the above simulated data along one representative direction. The L-HOSVD denoising with bases learned from the data with 5% noise produced images with obvious stripe artifacts. With bases learned from data with 3% noise levels, the L-HOSVD algorithm generated results with reduced artifacts. These results demonstrate that the artifacts are related to the HOSVD bases, and the L-HOSVD algorithm with bases learned from less noisy data can mitigate the artifacts. The bottom row

in Fig. 1 shows the reconstructed orientation distribution function (ODF), generated by using the 3DSlicer software (free available at www.slicer.org). The ODFs estimated from the images with severer artifacts are less accurate.

Based on the above findings, we proposed a GL-HOSVD algorithm which introduces a G-HOSVD denoising stage to prefilter the original images and then uses prefiltered images to guide the subsequent L-HOSVD denoising stage. The flow diagram of the GL-HOSVD algorithm is shown in Fig. 2, and the procedure of the GL-HOSVD algorithm is described in following subsections.

First stage of GL-HOSVD denoising

The global HOSVD stage, as enclosed by the blue dashed line in Fig. 2, employs the HOSVD transform by treating the DW images of all diffusion directions as a whole 3-order tensor. In this stage, the DW images are assumed to be effectively sparsified by the data-adaptive HOSVD bases. The small representation coefficients below a threshold τ_{global} are nullified to reduce noise. The threshold τ_{global} was set to $k_{global} \sigma \sqrt{2 \log(H \times W \times K)}$, where $k_{global} > 0$ is a scale that controls the smoothing degree in this stage, σ denotes the SD of the noise, H and W denote the height and width of images, respectively, and K denotes the number of diffusion directions.

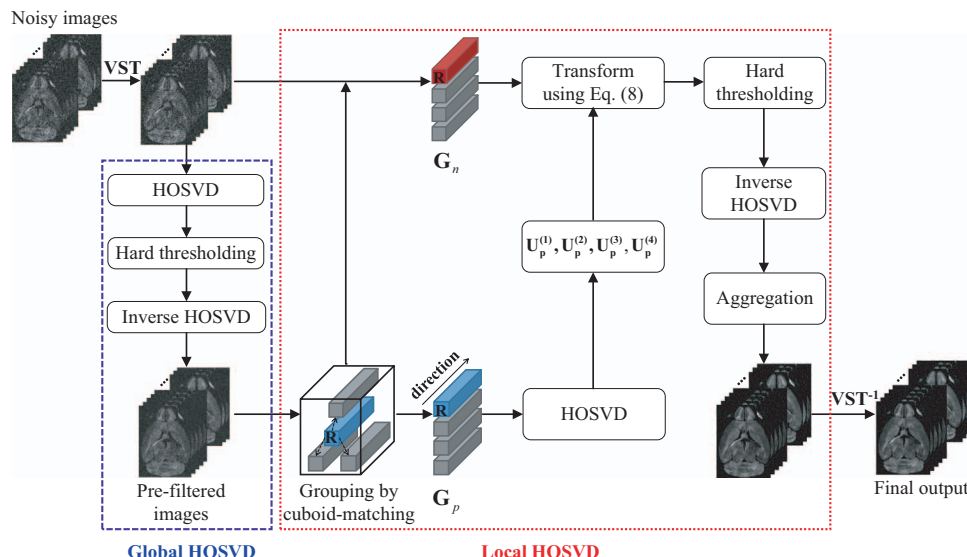


Fig. 2. Flow diagram of the proposed GL-HOSVD algorithm.

Second stage of GL-HOSVD denoising

The local HOSVD-denoising stage adopts a patch-based denoising approach similar to that in (Rajwade et al., 2013) and (Zhang et al., 2015a). As shown in the part enclosed by the red dotted line in Fig. 2, this stage involves the following steps: clustering similar patches or cubes into stacks, performing the HOSVD transform of each stack, hard thresholding the HOSVD coefficients, obtaining estimated stacks by inverting the HOSVD transform, and aggregating multiple estimates at each pixel to obtain the final denoised image.

In this stage, the size of the 3D patch was set to $m \times m \times K$, where m denotes the patch size in the spatial domain, and the patch size along the diffusion dimension is set to K , the number of diffusion directions. Thus, the search for similar 3D patches is performed across the 2D spatial domain. For brevity, the 3D patch is also called “cuboid” in this paper. Given the reference cuboid of size $m \times m \times K$, similar cuboids were found by searching and thresholding the photometric distance between two cuboids. To reduce the influence of noise on the cuboid grouping, we calculated the photometric distance on the global HOSVD prefiltered images to measure the dissimilarity between two cuboids as follows:

$$d(P_i, P_j) = \frac{\|P_i - P_j\|_2^2}{m^2 K} \quad (5)$$

where P_i and P_j denote the cuboids centered at pixels i and pixel j , respectively. $\|\cdot\|_2^2$ denotes the sum of squared differences between corresponding intensities of the two input cuboids, and $m^2 K$ is the number of pixels in a cuboid. Thus, cuboids with a distance below a predefined threshold were identified as similar to the reference cuboid:

$$S_i^{th} = \{j \in X_i : d(P_i, P_j) \leq \tau_d\} \quad (6)$$

where S_i^{th} denotes the coordinates set of clustered cuboids for the reference cuboid P_i , X_i denotes the search window centered at pixel i , and τ_d is the distance threshold. Similar to those in Rajwade et al. (2013) and Zhang et al. (2015a), the threshold was set to $3\sigma^2$ where σ represents the SD of the zero mean Gaussian noise. Let L denote the number of cuboids being identified as similar, we imposed a lower limit of $L \geq 30$ for effective denoising, and an upper limit of $L \leq 80$ for computation efficiency.

Given the coordinates set S_i^{th} , two groups of similar cuboids are constructed as shown in Fig. 2: one from the original noisy images and denoted as $G_n \in \mathbf{R}^{m \times m \times K \times L}$, and the other from the pre-filtered images and denoted as $G_p \in \mathbf{R}^{m \times m \times K \times L}$. The above matching step to group similar cuboids is similar to that in nonlocal means (NLM) (Buades et al., 2005) and BM3D (Dabov et al., 2007) algorithms. We hypothesize that the HOSVD bases learned from G_p are less affected by noise, compared with those learned from G_n . Thus, we propose to employ the HOSVD bases learned from G_p to transform G_n , instead of directly performing the HOSVD transform of G_n as in the conventional HOSVD-based denoising method (Rajwade et al., 2013; Zhang et al., 2015a).

The HOSVD transform of $G_p \in \mathbf{R}^{m \times m \times K \times L}$ is given by:

$$G_p = S_p \times_1 U_p^{(1)} \times_2 U_p^{(2)} \times_3 U_p^{(3)} \times_4 U_p^{(4)} \quad (7)$$

where $S_p \in \mathbf{R}^{m \times m \times K \times L}$ is a 4-order core tensor, $U_p^{(1)}, U_p^{(2)} \in \mathbf{R}^{m \times m}$, $U_p^{(3)} \in \mathbf{R}^{K \times K}$, and $U_p^{(4)} \in \mathbf{R}^{L \times L}$ are the orthogonal unitary matrices, with column vectors that can be considered as learned bases.

Afterward, G_n is projected onto the learned $U_p^{(1)}, U_p^{(2)}, U_p^{(3)}$, and $U_p^{(4)}$:

$$S_n = G_n \times_1 U_p^{(1)\top} \times_2 U_p^{(2)\top} \times_3 U_p^{(3)\top} \times_4 U_p^{(4)\top} \quad (8)$$

where $S_n \in \mathbf{R}^{m \times m \times K \times L}$ is a 4-order core tensor consisting of the transformed coefficients.

Then, S_n is manipulated by thresholding its elements using Eq. (3) with a threshold of $\tau_{local} = k_{local}\sigma\sqrt{2 \log(m \times m \times K \times L)}$, where $k_{local} > 0$ is a scale that controls the smoothing degree in this local HOSVD stage.

Let $\hat{S}_n \in \mathbf{R}^{m \times m \times K \times L}$ denote the thresholding results of tensor S_n , the denoised cuboid stack \hat{G}_n can be obtained by the following inverse transform:

$$\hat{G}_n = \hat{S}_n \times_1 U_p^{(1)} \times_2 U_p^{(2)} \times_3 U_p^{(3)} \times_4 U_p^{(4)}. \quad (9)$$

The above operations with Eqs. (5)–(9) are implemented in a sliding window manner across the whole image domain with a step size of N_{step} . A small sliding step usually corresponds to more accurate denoising but at the cost of increased computation burden. Thus, N_{step} is usually determined by balancing denoising accuracy and efficiency.

Finally, the multiple estimates of each pixel are aggregated to obtain the denoised image using the following rule:

$$\hat{x}_i = \frac{\sum_{j=1}^V \theta_j \sum_{k=1}^{K_j} \hat{G}_j^k(i)}{\sum_{j=1}^V K_j \theta_j}, \quad \theta_j = \frac{1}{1 + \|\hat{S}_j\|_0} \quad (10)$$

where \hat{x}_i is the estimated value at pixel i after aggregation, $\hat{G}_j^k(i)$ the value of pixel i on the k th cuboid from the group \hat{G}_j , K_j the number of cuboids containing the pixel i in the group \hat{G}_j , V the number of groups containing pixel i , and θ_j the weight of each group \hat{G}_j . θ_j is set inversely related to $\|\hat{S}_j\|_0$, which equals to the number of nonzero coefficients in the core tensor \hat{S}_j of the group \hat{G}_j after the thresholding operation.

In the proposed GL-HOSVD algorithm, the global HOSVD stage can improve the subsequent local HOSVD stage in two aspects. First, grouping cuboids in the prefiltered images would be more accurate because of the reduced noise effect. Furthermore, the HOSVD bases learned from prefiltered images are less corrupted by noise, and thus may help to mitigate stripe artifacts in the local HOSVD denoising. The contribution of the global HOSVD stages depends on the threshold τ_{global} . When τ_{global} decreases to zero, the proposed GL-HOSVD algorithm reduces to a one-stage local HOSVD denoising algorithm.

The adaption to non-Gaussian noise in DW magnitude images

The above HOSVD-based denoising algorithm is designed for data corrupted with additive white Gaussian distributed noise. It cannot be directly applied to denoising MR magnitude images in which noise usually follows Rician (Bernstein et al., 1989; Henkelman, 1985) or noncentral Chi distribution (Aja-Fernandez and Tristan-Vega, 2012; Constantinides et al., 1997; Dietrich et al., 2008). For the application of the GL-HOSVD algorithm to denoising DW magnitude images, the forward variance-stabilizing transformation (VST) proposed by Foi (2011) is used to stabilize the non-Gaussian noise into noise with uniform SD across the image, as shown in Fig. 2. After the GL-HOSVD denoising, inverse VST is performed to obtain the unbiased estimate from the filtered data. Let Z denote a MR magnitude data corrupted by the Rician or noncentral Chi noise, the integration of VST and the GL-HOSVD algorithm can be represented as follows:

$$\hat{X} = VST^{-1}(GL-HOSVD(VST(Z, \sigma_n), \sigma_{VST}), \sigma_n) \quad (11)$$

where \hat{X} denotes the denoised data, σ_n the SD of complex Gaussian noise for MR magnitude data Z , σ_{VST} the SD of the DW images after VST and generally stabilized to one, and VST^{-1} the inverse VST applied on the denoised data to return a maximum-likelihood estimate of the noise-free magnitude. In the simulation, σ_n was set the predefined value of the SD of the noise. In the in vivo experiments, σ_n was calculated from the background intensities.

Experiments and results

Simulated data

To quantitatively evaluate the performance of denoising algorithms, DW images were synthesized by using the tensor model $S_0 \exp(-bg^T \mathbf{D}g)$, where S_0 is the non-diffusion signal, \mathbf{g} a unit gradient vector, and \mathbf{D} the diffusion tensor. An adult mouse diffusion tensor

atlas from the Biomedical Informatics Research Network Data Repository as in (Lam et al., 2014) was used for simulation. Forty-five DW images with size of 256×256 were generated including one with $b=0$ and forty-four with $b=2000 \text{ s/mm}^2$ along varying gradient directions randomly distributed on unit sphere. The noisy images were obtained by adding zero-mean Gaussian distributed noise to both real and imaginary parts of the noise-free images, and the final magnitude image was obtained by the root-sum-square operation as follows:

$$\mathbf{I}_n = \sqrt{\sum_{c=1}^C [(\mathbf{I} + \mathbf{N}_{1c})^2 + (\mathbf{N}_{2c})^2]} \quad (12)$$

where \mathbf{I} denotes the noise-free DW images, \mathbf{N}_{1c} and \mathbf{N}_{2c} the Gaussian noise with a SD of σ_n , and C the number of coils. The noisy magnitude images follow the Rician distribution if $C=1$ and noncentral Chi distribution if $C > 1$. In our experiment, the images with the noncentral Chi noise were simulated with $C=4$. To evaluate the performance under different noise levels, the maximum intensities of the simulated DW data at $b=0$ were normalized to 1, and the noise was synthesized with σ_n varying from 0.01 to 0.1 with an increment of 0.01. Given the same σ_n , the SNR of the DW data with the noncentral Chi noise at $C=4$ was twice that of DW data with the Rician noise.

Experimental data

The effectiveness of the proposed method on real DW images was verified on three in vivo brain DW datasets from healthy volunteers. For the first two datasets, we selected a representative slice of images in denoising experiment, for the consistency with the simulation experiment. The third dataset was used to validate the application of GL-HOSVD to volume DW data.

The first dataset was collected on a 3T Siemens scanner (Trio, Siemens Healthcare USA) using a 32-channel receiver head coil. The data was minimally processed with bipolar echo planar imaging (EPI) correction (a linear phase correction) and reconstructed by partial Fourier reconstruction (Haldar et al., 2009). Diffusion encodings along 30 directions with $b=1000$, 2000, and 3000 s/mm^2 were acquired. In addition, one image with $b=0$ was obtained. The imaging parameters were as follows: TR/TE=3600/98 ms, in-plane resolution= $2 \times 2 \text{ mm}^2$, slice thickness=2 mm, matrix size= 256×256 , slices=35, and number of excitations (NEX)=1.

The second and the third DW brain datasets were both acquired on a Philips 3.0T TX MR scanner (Achieva, Philips Medical Systems, Best, The Netherlands) with 4-shot EPI sequence using an 8-channel receiver head coil. The images were reconstructed by using multiplexed-SENSE reconstruction without acceleration factor (Chen et al., 2013; Zhang et al., 2015b). The imaging parameters of the second dataset were: 6 diffusion directions with $b=1000 \text{ s/mm}^2$ and a $b=0$ image, TR/TE=3000/82 ms, in-plane resolution= $1 \times 1 \text{ mm}^2$, slice thickness=4 mm, matrix size= 220×220 , slices=14, and the scan was repeated 10 times for a high SNR reference (NEX=10). The imaging parameters of the third dataset were: 15 diffusion directions with $b=1000 \text{ s/mm}^2$ and a $b=0$ volume, TR/TE=17,000/80 ms, resolution= $1.5 \times 1.5 \times 1.5 \text{ mm}^3$, volume size= $148 \times 148 \times 90$ and NEX=1.

Evaluation measures

In the presence of noise-free reference, the quality of the denoised DW images is evaluated in terms of the peak SNR (PSNR). For the simulated DW images with the maximum intensity of 1, the PSNR is defined via the mean squared error (MSE) between the noise-free data and denoised data as follows:

$$\text{PSNR} = 10 \log_{10} \left(\frac{1}{\text{MSE}} \right) \quad (13)$$

The PSNR is calculated on the DW images of all directions and the image with zero b value.

To get further insights into the effect of denoising on the diffusion tensor quantification, we also provided: (i) the root-mean-squared-error (RMSE) of the fractional anisotropy (FA), shorted as FA-RMSE, (ii) the RMSE of mean diffusivity (MD), shorted as MD-RMSE and (iii) the mean Frobenius distance between two tensor-fields, shorted as **Tensor-Fro.dist**. The tensors were estimated based on the linear least squares method for log-transformed signals. We excluded the voxels with the lowest signal from the calculation of tensors for simulation. All the above quantitative metrics were calculated in the anatomical region with background removed.

Implementation of GL-HOSVD

In the implementation of the proposed GL-HOSVD algorithm (<https://github.com/XinyuanZhang719/gl-hosvd>), there are five free parameters including the patch size m , search window size N_s , step length N_{step} , scales k_{global} and k_{local} in the thresholds. These parameters were empirically determined using the following strategy.

For the simulation and the first two in vivo datasets, the patch size m of 8, search window size N_s of 11, and step length N_{step} of 5 were found to produce good results with minimum stripe artifacts in the local HOSVD denoising stage. For the implementation of GL-HOSVD on the 3D in vivo data with 3D isotropic resolution, we set the cube size m as 4, search window size N_s as 5, and step length N_{step} as 3 for the third in vivo dataset. Note that the patch size m , search window size N_s , and step length N_{step} are the common parameters in the transform-based denoising algorithms (Dabov et al., 2007; Dong et al., 2013; Maggioni et al., 2013; Zhang et al., 2015a), and the empirical selection of these three parameters can produce satisfactory results.

For the simulation experiments, the k_{global} and k_{local} settings in the thresholds were determined with reference to the noise-free images. The proposed GL-HOSVD method was implemented with varying k_{global} and k_{local} , and the resulting PSNR and FA-RMSE values were adopted as the quantitative measures to analysis the influence of k_{global} and k_{local} on the denoising performance. The PSNR and FA-RMSE values were plotted against varying k_{global} in Fig. 3, and k_{local} in Fig. 4. As seen from Figs. 3 and 4, k_{global} of 0.4 and k_{local} of 1 produced a approximately optimal result in terms of PSNR and FA-RMSE for the varying noise levels in the case of Rician and noncentral Chi noise. Thus, k_{global} and k_{local} were fixed at 0.4 and 1 in the following simulation experiments, although these two values are not strictly optimal for each noise level. For the in vivo experiments, k_{global} of 0.4 in the simulation was directly transferred to denoising in vivo data, and k_{local} is determined by inspecting the visual quality of denoised images and quantified FA maps.

Algorithm validation

To validate the effect of introducing the global HOSVD prefiltering stage to the local HOSVD method, we compared the proposed GL-HOSVD method with the following HOSVD-based methods using simulation: 1) G-HOSVD, a one-stage global HOSVD denoising algorithm; 2) L-HOSVD, a patch-based one-stage HOSVD denoising algorithm; 3) L-HOSVD-W, a wiener filter-augmented two-stage HOSVD denoising algorithm (Rajwade et al., 2013); and 4) L-HOSVD-R, a regulation-augmented two-stage HOSVD denoising algorithm in which the second stage is the HOSVD denoising of the combined image from original and pre-denoised images (Zhang et al., 2015a). The HOSVD-based denoising algorithms used in our paper and corresponding parameters are summarized in Table 1.

The patch size m , step length N_{step} , and search window size N_s , in the three local HOSVD algorithms (L-HOSVD, L-HOSVD-W, and L-HOSVD-R) were set to be similar to those of the GL-HOSVD algorithm. The L-HOSVD-R algorithm involves two additional parameters: the relaxation parameter ξ that represents the part of the original noisy images in the combined image, and the scaling factor γ that controls

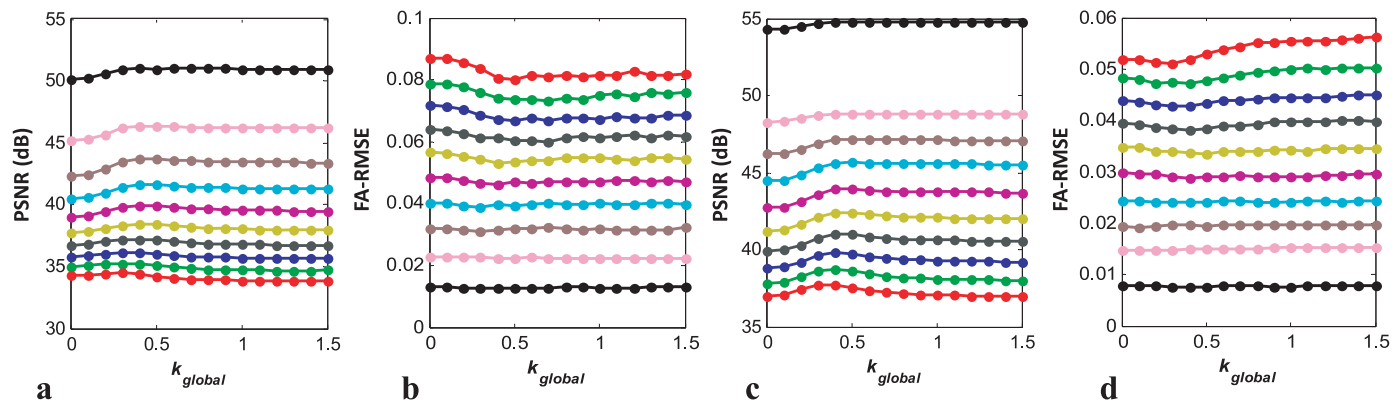


Fig. 3. Influence of the parameter k_{global} in the GL-HOSVD algorithm under varying noise levels for simulated data. (a-b) Rician and (c-d) noncentral Chi distributed data. The curves from top to bottom (a, c) and from bottom to top (b, d) respectively correspond to the SDs varying from 0.01 to 0.1 increased by 0.01.

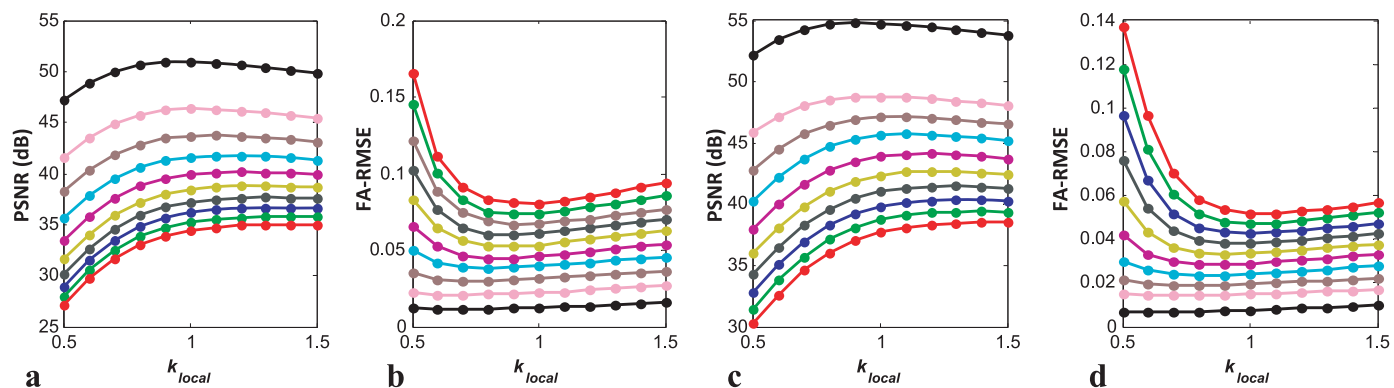


Fig. 4. Influence of the parameter k_{local} in the GL-HOSVD algorithm under varying noise levels for simulated data. (a-b) Rician and (c-d) noncentral Chi distributed data. The curves from top to bottom (a, c) and from bottom to top (b, d) respectively correspond to the SDs varying from 0.01 to 0.1 increased by 0.01.

the re-estimation of noise in the combined images. The parameters ξ and γ were set to 0.38 and 0.65, respectively, as suggested by Zhang et al. (2015a). For a fair comparison, the local thresholds in all the HOSVD-based algorithms were optimized in terms of PSNR.

Fig. 5 compares the proposed GL-HOSVD algorithm with the four HOSVD variants (G-HOSVD, L-HOSVD, L-HOSVD-W, and L-HOSVD-R), using simulated DW data. Fig. 5a shows the noise-free DW image at $b=2000 \text{ s/mm}^2$, and Fig. 5b the image corrupted by the Rician noise with an SD of $\sigma_n = 0.05$. G-HOSVD image contain serious residual noise. The three local HOSVD algorithms significantly reduce noise in the images with well preserved edges, but with stripe artifacts in smooth regions as pointed by the arrows in the enlarged views. In contrast, the stripe artifacts are significantly reduced in the GL-HOSVD image. Fig. 5h plots the PSNR of HOSVD-based denoising algorithms on simulated DW data against varying SDs (σ_n) from 0.01 to 0.1 with an increment of 0.01. G-HOSVD yields the minimum PSNR values, and

the GL-HOSVD outperforms the three local HOSVD algorithms in terms of PSNR. The effect of these stripe artifacts on diffusion tensor quantification is demonstrated in Fig. 6. The stripe artifacts in the L-HOSVD image leads to similar artifacts in the corresponding FA map. No obvious stripe artifact can be observed in the FA map quantified from GL-HOSVD images.

Comparison with other DW image denoising algorithms

We compared the proposed GL-HOSVD algorithm with two recently proposed state-of-the-art DW image denoising methods: NLM with bias correction (Wiest-Daessle et al., 2007), and the low rank with edge constraint method (LR+Edge) (Lam et al., 2014). The implementation of the two algorithms is described as follows.

- 1) The NLM with bias correction was applied to separately denoise

Table 1

Summary of the HOSVD-based denoising algorithms and corresponding parameters.

Algorithms	Algorithms description	Parameters description
GHOSVD	One-stage denoising. A simple global HOSVD denoising which treats the whole images as a single tensor	Global threshold related k_{global} .
LHOSVD	One-stage denoising. A simple patch-based HOSVD denoising	Patch size m , step length N_{step} , search window size N_s , and the local threshold-related k_{local} .
LHOSVD-W	Two-stage denoising. The first stage is a patch-based HOSVD denoising, and the second stage is a wiener filter.	Patch size m , step length N_{step} , search window size N_s , and the local threshold-related k_{local} .
LHOSVD-R	Two-stage denoising. Both stages are patch-based HOSVD denoising.	Patch size m , step length N_{step} , search window size N_s , local threshold-related k_{local} , relaxation parameter ξ , and the scaling factor γ
GLHOSVD	Two-stage denoising. The first stage is a global HOSVD, and the second stage is a patch-based HOSVD.	Patch size m , step length N_{step} , search window size N_s , global threshold-related k_{global} , and the local threshold-related k_{local} .

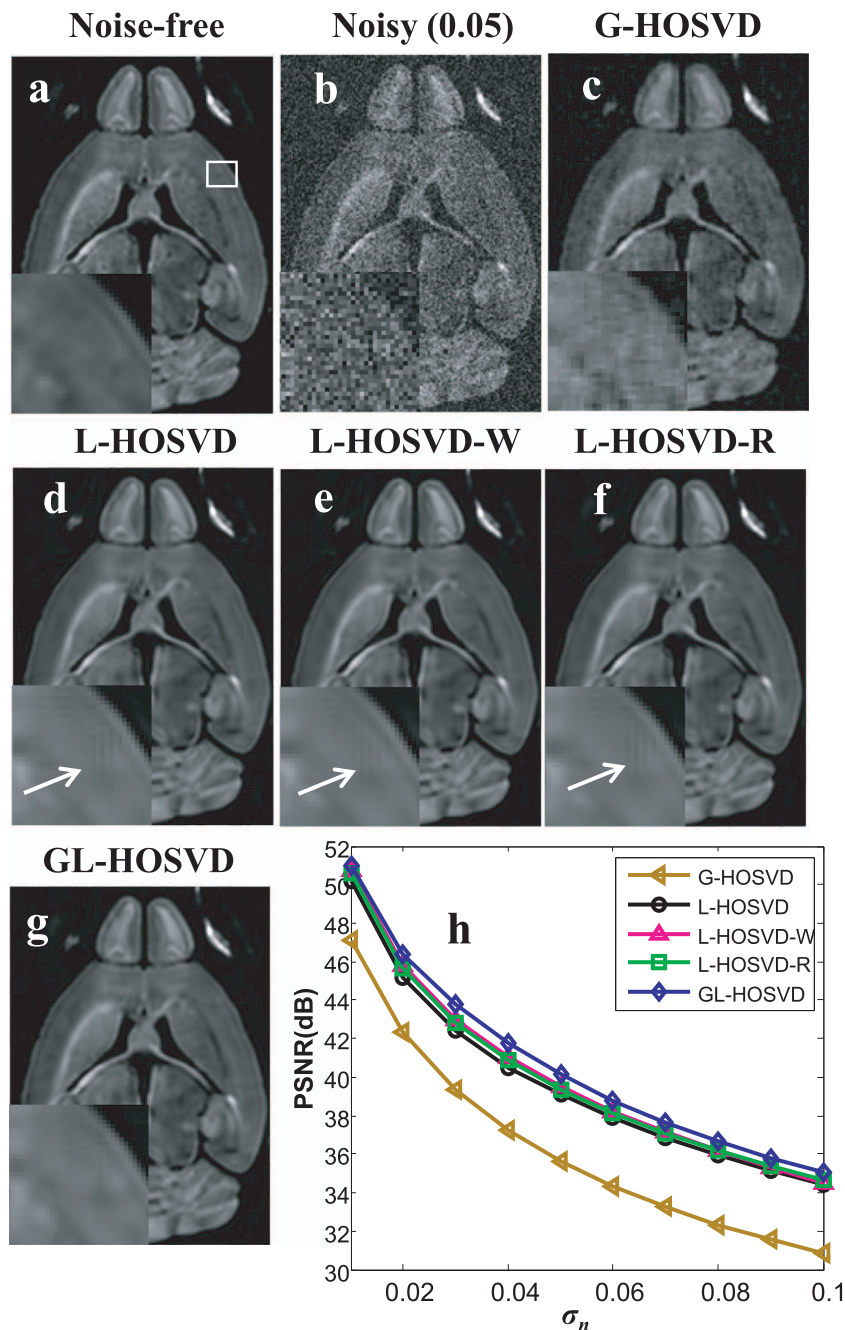


Fig. 5. Comparative results between G-HOSVD, L-HOSVD, L-HOSVD-W, L-HOSVD-R, and the proposed GL-HOSVD algorithms. The noise-free image is the DW image along a representative direction at $b=2000 \text{ s/mm}^2$. The noisy image contains Rician noise with $\sigma_n=0.05$. The PSNR was calculated using DW images along all directions and at all b -values.

DW images along different directions, as suggested by Wiest-Daessle et al. (2007). The NLM method was implemented by ourselves according to the implementation details of Wiest-Daessle et al. (2007). The patch size and search window were fixed at 5 and 11, respectively, same to those in (Manjon et al., 2008). In the simulation experiments, the smooth controlling parameter [h] in Eqs. (2) and (3) as described by Manjon et al. (2008)] was adjusted with an exhaustive search in a certain range to produce the optimal PSNR value under each noise level. In the in vivo data experiments, this parameter was manually adjusted by the visual inspection of the filtered images.

2) The LR+Edge integrates the Rician/noncentral Chi likelihood model, the low-rank model and the edge prior into an maximum a posteriori estimation framework and uses an alternating mini-

mization algorithm to solve the associated optimization problem. The LR+Edge method was implemented by using the source code from Lam et al. (2014). The simulation and the first in vivo dataset were denoised by using the original parameters setting in (Lam et al., 2014), which were shown to produce quantitative results close to that reported in that paper.

Comparison results using simulation data

In Figs. 7–11, we compare the proposed GL-HOSVD algorithm with the NLM and LR+Edge algorithms on simulated DW data with Rician and noncentral Chi noise. The GL-HOSVD was implemented with $k_{local}=1.0$.

Fig. 7 shows the quantitative comparison of the simulated DW data

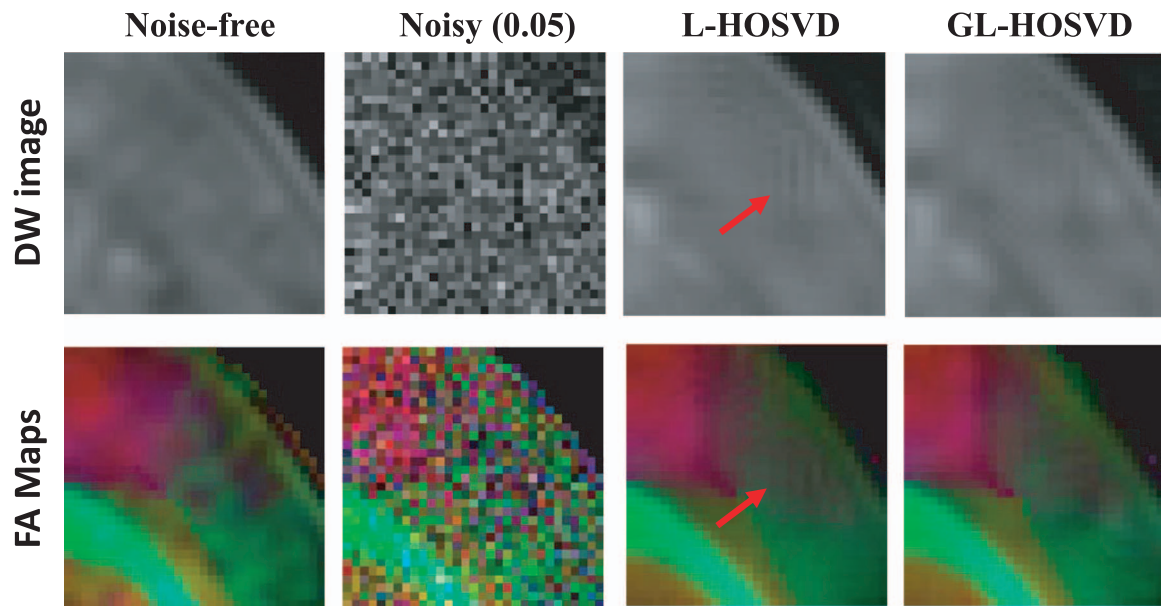


Fig. 6. Comparison of FA maps from DW images filtered by L-HOSVD and GL-HOSVD. Top row shows enlarged images in the squares of Fig. 5. Bottom row shows the corresponding color-coded FA maps. The color is based on the orientation of the primary eigenvector of diffusion tensor: red for right-left, green for anterior-posterior, and blue for inferior-superior.

denoised by the three algorithms under varying noise levels with σ_n from 0.01 to 0.1 with an increase of 0.01. GL-HOSVD consistently outperforms the other two algorithms in terms of all the four quantitative metrics. Specifically, the PSNR of GL-HOSVD increased by $\sim 14\%$ compared with that of NLM, and $\sim 5\%$ compared with that of LR+Edge. The FA-RMSE, MD-RMSE and `Tensor-Fro.dist` of GL-HOSVD algorithm respectively decreased by $\sim 40\%$, $\sim 48\%$, $\sim 37\%$ compared with the NLM algorithm, and $\sim 27\%$, $\sim 30\%$, $\sim 25\%$ compared with the LR+Edge algorithm.

Figs. 8 and 9 show the denoised DW images at $b=2000 \text{ s/mm}^2$ with one representative encoding direction, fitted FA maps, color-coded FA maps, and their corresponding error maps, under the Rician and noncentral Chi noise with $\sigma_n = 0.05$. All the three algorithms significantly reduce the noise in the image, but GL-HOSVD preserves better details than NLM and LR+Edge. The GL-HOSVD image is visually closest to the noise-free image, which is consistent with the quantitative PSNR analysis in Fig. 7. The FA and color-coded FA maps from the GL-HOSVD images are closer to the reference maps than those obtained from the NLM and LR+Edge images. Fig. 10 presents the ODFs estimated from the data in the white boxes as shown in Figs. 8 and 9. The ODFs from the GL-HOSVD images are closer to those from the noise-free images, compared with those from the NLM and LR+Edge images. Fig. 11 presents the FA quantification errors for NLM, LR+Edge and GL-HOSVD algorithms. The FA errors of LR+Edge and GL-HOSVD are more concentrated around zeros with smaller bias (dashed line) and narrower variance (solid line), compared with that of NLM. The bias and variance in the FA errors of GL-HOSVD are slightly lower than those of LR+Edge, and this indicates that the GL-HOSVD denoised images preserve well the anisotropy of diffusion tensors.

Comparison results using *in vivo* data

In Figs. 12 and 13, we compare the three algorithms using the first brain dataset with $b=1000$, 2000 , and 3000 s/mm^2 , which was also used by Lam et al. (2014). The images with different b-values and gradient directions were filtered independently in the implementation of the NLM algorithm, whereas images of all b-values and gradient directions were simultaneously filtered in the implementation of the LR+Edge and GL-HOSVD algorithms. The three algorithms were performed to denoise the DW images coil by coil, and the final result was obtained using the sum-of-squares operation on the denoised coil

images, similar to the procedure by Lam et al. (2014) for a fair comparison. Fig. 12 presents the denoised images and corresponding image residuals, and Fig. 13 shows the FA maps and color-coded FA maps. The main structures in the original image are seriously degraded by noise, especially at high b-values. The three algorithms significantly reduced the noise and GL-HOSVD yields images with more clearly defined details and less remnant noise, compared to NLM and LR+Edge. The image residuals of LR+Edge and GL-HOSVD show visible anatomical information, which consists mainly of removed SNR-related bias caused by the noncentral Chi noise. The FA and color-coded FA maps from the GL-HOSVD images have less remnant noise compared with NLM and LR+Edge algorithms.

Both the GL-HOSVD and NLM algorithms were applied to high-spatial resolution DW images, with the reference image acquired with $\text{NEX}=10$. The LR+Edge algorithm was not compared because the low rank property in this algorithm is not suitable for denoising the DW images with such a small number of directions. The comparison result of a representative slice is shown in Fig. 14. GL-HOSVD preserves well the rapid-changing details while suppressing noise. As indicated by the regions enclosed by the blue squares, the NLM image displays slightly blurred structures, while the GL-HOSVD image demonstrates a better preservation of details and is closer to the reference image. The FA maps from the NLM and GL-HOSVD images are less affected by noise and visually close to that from reference images. Both NLM and GL-HOSVD effectively recover the original ODFs in most regions, but NLM induces a swelling effect and perturbs the diffusion directions in several locations.

To verify the effectiveness of the proposed GL-HOSVD algorithm on the volume DW data at multiple directions, the GL-HOSVD was implemented on the third *in vivo* dataset with two versions: (i) filtering the images with multiple directions slice by slice in the same way as for the simulation and the first two *in vivo* datasets, termed as GL-HOSVD¹ and (ii) filtering the volume data with multiple directions together by performing the 4-order HOSVD transform in the global denoising stage and the 5-order HOSVD transform in the local denoising stage, termed as GL-HOSVD². Fig. 15 shows the effect of denoising on a representative slice and the reconstructed fibers. Both GL-HOSVD¹ and GL-HOSVD² significantly reduce noise and preserve the details well. The GL-HOSVD² image is more visually pleasant with clearer edges than the GL-HOSVD¹ image, which can be easily observed in the regions enclosed by the blue squares. The fibers

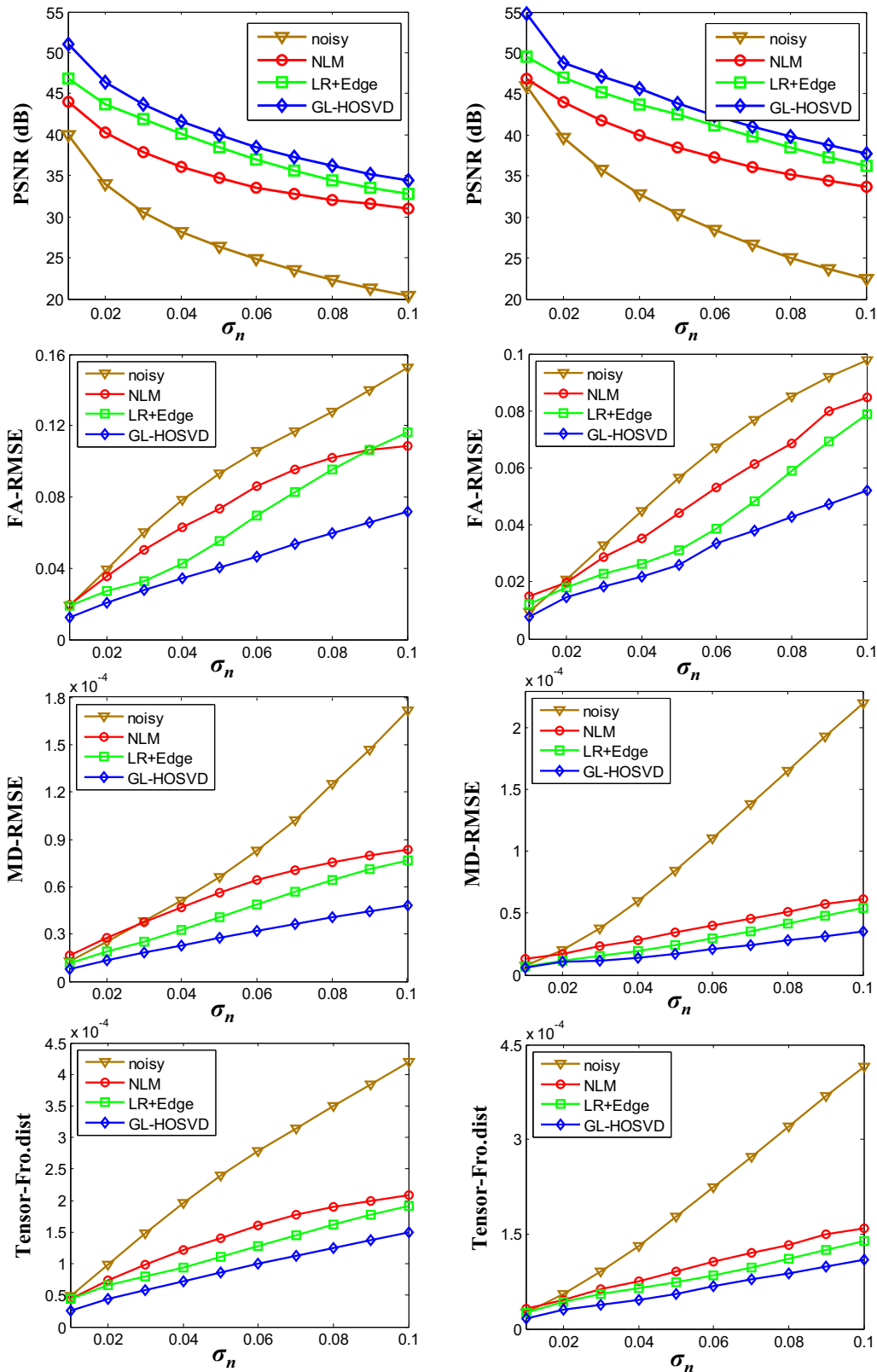


Fig. 7. Quantitative comparison of the NLM, LR+Edge and GL-HOSVD algorithms under varying σ_n using simulated data. Left column: Rician noise. Right: noncentral Chi (Coils=4) noise.

tracked from the original noisy data are rare and not well organized, whereas the fibers from the denoised data are richer and well-organized. The fibers tracked from the GL-HOSVD² images are slightly richer and smoother than those from the GL-HOSVD¹ images, as shown in the region enclosed by the red squares.

Discussion and conclusion

This paper investigates the feasibility of denoising DW images by using the HOSVD transform. We developed a novel approach which employs a global HOSVD prefiltering stage to guide the conventional

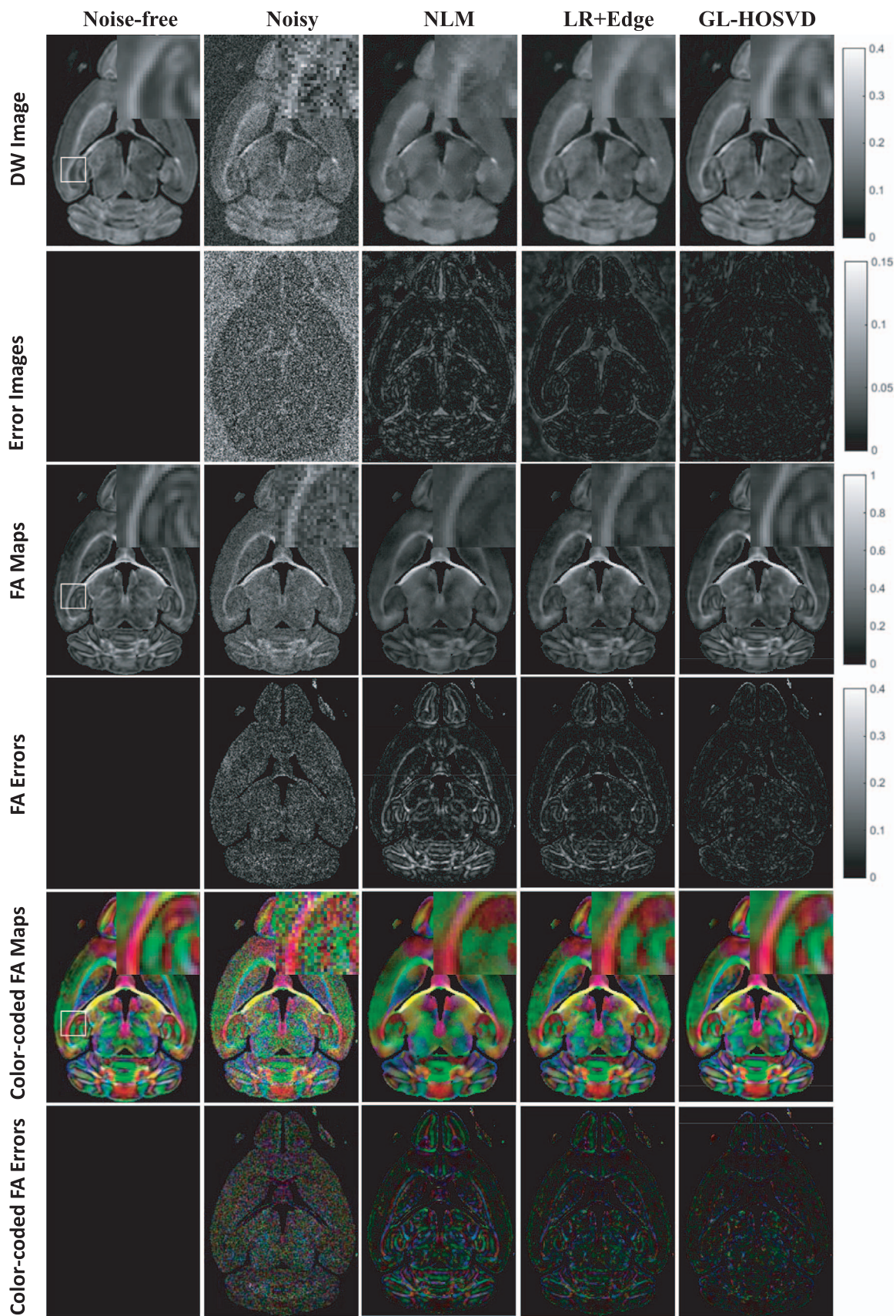


Fig. 8. Denoising results of the NLM, LR+Edge, and GL-HOSVD algorithms for simulated DW data with the Rician noise ($\sigma_n=0.05$). The DW image along a representative direction at $b=2000 \text{ s/mm}^2$ was presented. The error images show the absolute difference between denoised and noise-free images. The FA errors show the absolute difference between FA maps calculated from denoised and noise-free images. The color is based on the orientation of the primary eigenvector of diffusion tensor: red for right-left, green for anterior-posterior, and blue for inferior-superior.

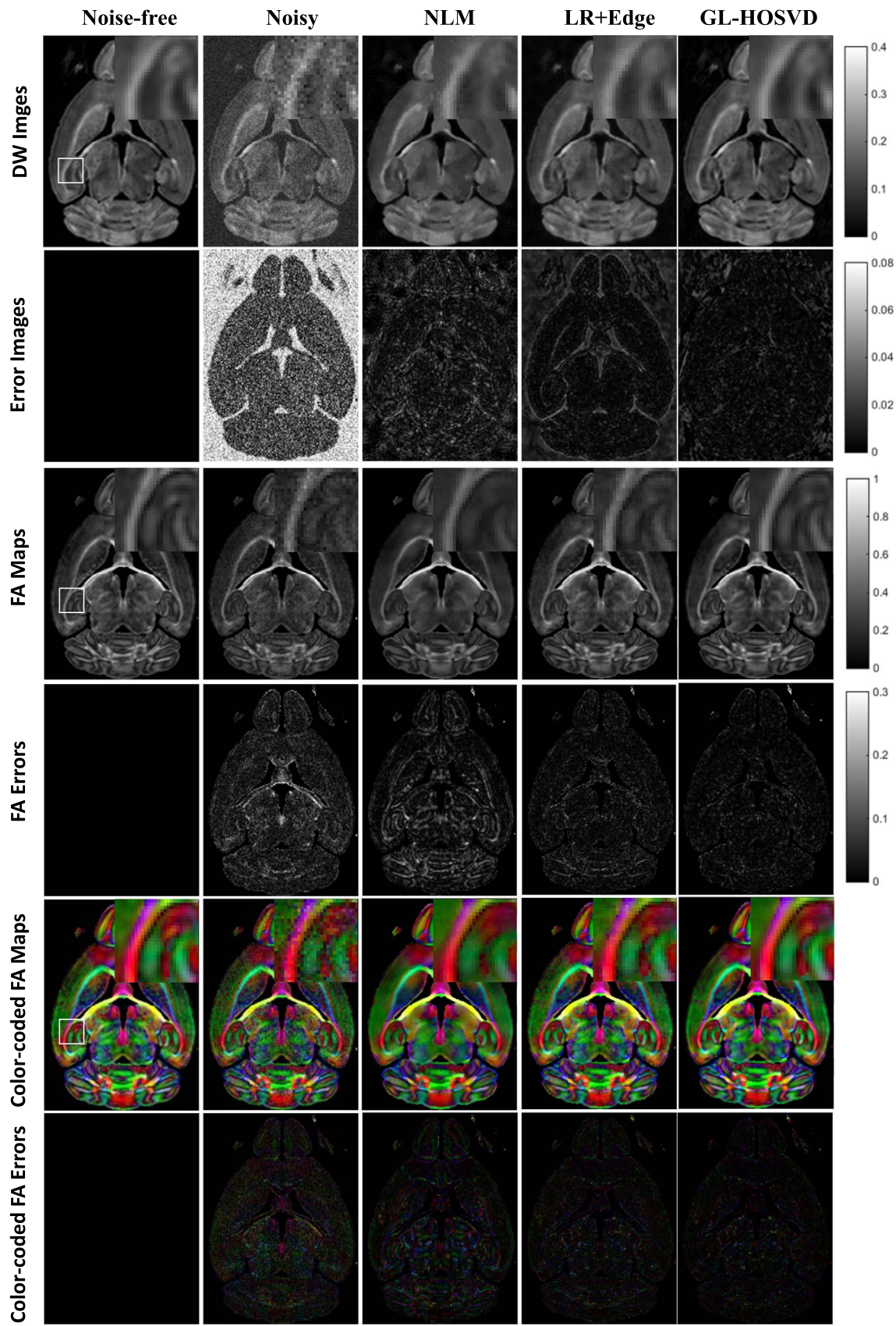


Fig. 9. Denoising results of the NLM, LR+Edge, and GL-HOSVD algorithms for simulated DW data with the noncentral noise ($\sigma_n=0.05$). The DW image along a representative direction at $b=2000 \text{ s/mm}^2$ was presented. The error images show the absolute difference between denoised and noise-free images. The FA errors show the absolute difference between FA maps calculated from denoised and noise-free images. The color is based on the orientation of the primary eigenvector of diffusion tensors: red for right-left, green for anterior-posterior, and blue for inferior-superior.

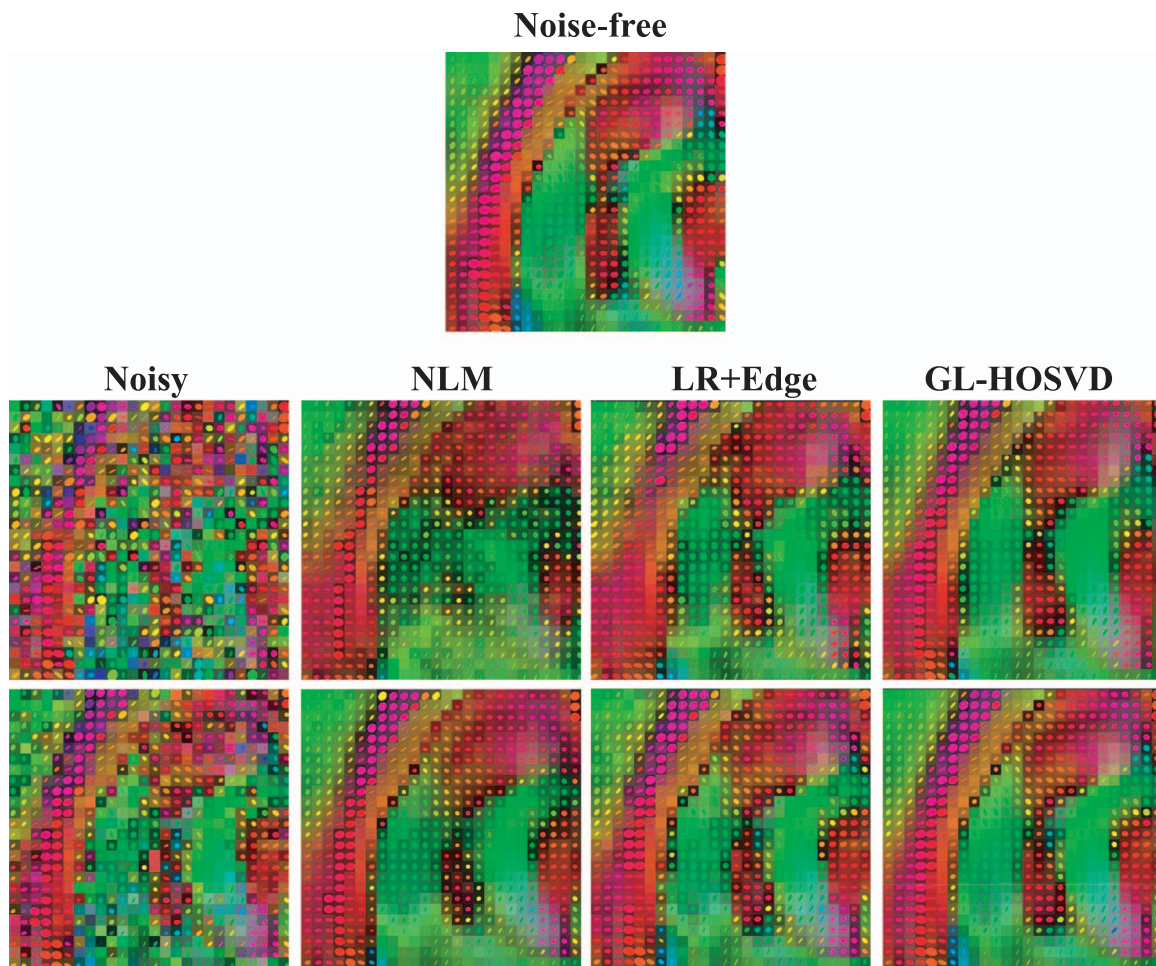


Fig. 10. The corresponding reconstructed ODFs in the white box of Figs. 8 and 9. The second row and bottom row show the results for Rician and noncentral Chi distributed data, respectively.

local HOSVD denoising algorithm. The proposed GL-HOSVD algorithm can successfully mitigate stripe artifacts produced by the local HOSVD denoising algorithm. GL-HOSVD can simultaneously exploiting information redundancy across spatial domain and along diffusion directions using the HOSVD transform. The experiments on simulation and in vivo DW data demonstrate that GL-HOSVD outperforms two state-of-the-art DW image denoising methods in terms of denoising quality and estimation of diffusion parameters.

In GL-HOSVD, the local HOSVD stage employs a popular framework in image denoising domain, namely, grouping similar patches, denoising grouped patches and aggregating (Dabov et al., 2007; Dong et al., 2013). The denoising methods based on this framework are approaching to theoretical limits of image denoising (Chatterjee and Milanfar, 2010; Knaus and Zwicker, 2014; Levin and Nadler, 2011). Thus, the combination of this framework with the HOSVD transform enables effective denoising. However, as observed in our experimental results, this local HOSVD denoising algorithm suffers from visible stripe artifacts. We demonstrated that these artifacts are caused by the noise-deteriorated HOSVD bases learned from the grouped patches affected by severe noise. To mitigate these artifacts, we introduced a G-HOSVD denoising stage to prefilter images. The prefiltered image was used to group similar patches and train HOSVD bases in the following L-HOSVD denoising stage. Although in theory any filter algorithm can be used for prefiltering, in fact we had tried several well-known filtering algorithms including the nonlocal means (Manjon et al., 2008) and patch-based HOSVD (Rajwade et al., 2013; Zhang et al., 2015a), and found that prefiltering by G-HOSVD yielded best denoising performance.

Similar to most denoising methods, the performance of GL-HOSVD depends on filtering parameters. Among the free parameters of GL-HOSVD, the patch size, search window size and step length are the most common parameters as in other transform-based denoising methods (Dabov et al., 2007; Dong et al., 2013; Maggioli et al., 2013; Zhang et al., 2015a), and the empirical selection of these three parameters usually produces satisfactory results. The remaining two parameters are threshold-related k_{global} and k_{local} . The results demonstrate that the selection of optimal k_{global} and k_{local} is robust to the noise levels. The parameter k_{global} which can produce a prefiltered image with higher accuracy does not necessarily imply more accurate final denoised results. Actually, a less smoothing prefiltered image with small k_{global} is preferred to produce a more accurate final denoising results. Note that quantitative evaluation is generally impossible for in vivo data because of unknown truth. Thus, filtering parameters are usually manually and carefully tuned according to image contents in practice. Optimal and automatic determination of filtering parameters could be further investigated by combining the proposed method with objective metrics such as Stein's unbiased risk estimate (Stein, 1981) and the no-reference metric Q (Zhu and Milanfar, 2010) when gold standard reference is unavailable in practice.

The GL-HOSVD algorithm is first designed for data corrupted by additive white Gaussian noise, and then combined with the VST transform to enable the application to denoising DW magnitude images with spatially-invariant Rician/noncentral Chi noise. It is well known that the impact of noise on MR magnitude images is SNR dependent. The VST can successfully stabilize the noise variance in the magnitude into one, i.e., the noise in VST-transformed data is no longer SNR

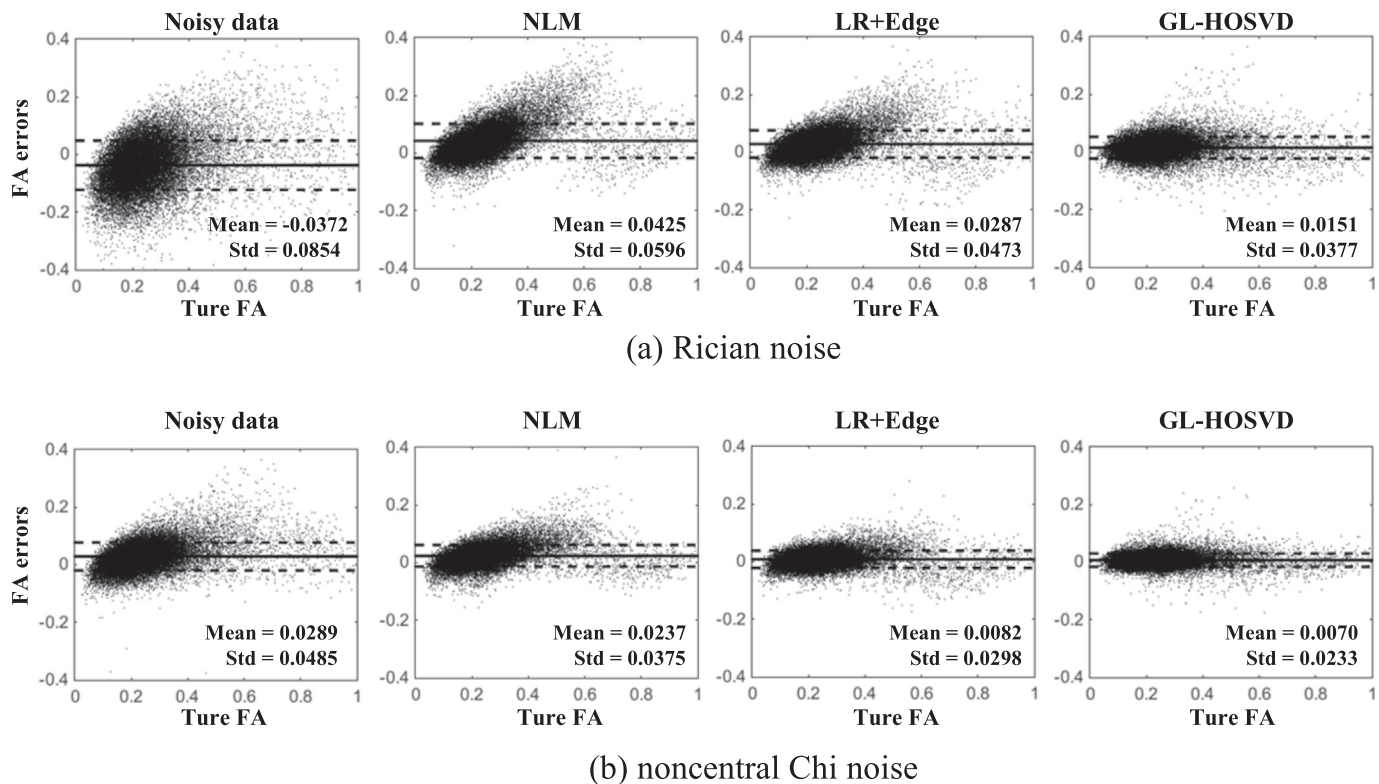


Fig. 11. Quantitative comparison of FA estimation for simulated data with noise level of $\sigma_n=0.05$. (a) Rician and (b) noncentral Chi distributed data. The bias (dash line) and the standard deviation (solid line) are also shown.

dependent. The signal transformation framework proposed by Koay et al. (2009a) can also be used to directly transform the Rician or noncentral Chi signals to unbiased Gaussian signals with the advantage of not requiring the bias correction after image denoising. The reconstruction of clinical DW data usually involves preprocessings to correct eddy current, ghost and geometric distortion, partial k-space reconstructions, and parallel imaging reconstructions, which may introduce spatial correlations and change the noise distribution in images. Thus, the good performance of the GL-HOSVD method on the simulation data with well-defined noise distribution does not imply that the proposed method can work naturally on clinical data in which the noise characteristic is not well theoretically defined. Note that the noise level in DW images is generally spatially-variant when images are reconstructed by using parallel imaging techniques such as sensitivity encoding (SENSE) (Pruessmann et al., 1999) and generalized auto-calibrating partially parallel acquisitions (GRAPPA) (Griswold et al., 2002). To deal with such spatially-variant Rician or noncentral Chi noise, the VST can be combined with the noise level map, which can be obtained by using local noise estimation methods (Koay et al., 2009b; Manjón et al., 2010; Manjón et al., 2015; Veraart et al., 2015). Another potential approach to address the problem of spatial varying noise levels is to estimate noise by analyzing the coefficients after the HOSVD transform in a similar way as in (Manjón et al., 2015).

In denoising multi-shell DW images data, simultaneous filtering of multiple b-value images was shown to outperform separate filtering of each b-value image (Becker et al., 2014), and the same approach was adopted in the application of GL-HOSVD to denoise *in vivo* data with $b=1000$, 2000, and 3000 s/mm^2 . This approach assumes that the DW images at multiple b-values are well spatially aligned. Registration can realign DW images but will introduce spatial correlation. In addition, severe noise in the high-b-value image may decrease the accuracy and robustness of registration. Thus, applying GL-HOSVD before registration may seem preferable in the presence of small displacements which generally hold in practice.

Note that GL-HOSVD cannot be applied to reduce the physiological

noise in diffusion MRI. The physiological noise mainly derives from breathing and cardiac-induced pulsative motion (Chang et al., 2012). To the best of our knowledge, the suppression of physiological noise in diffusion MRI data is rarely reported and still an open question. Several diffusion models have been proposed to reduce the effect of physiological noise on parameter estimation (Chang et al., 2012; Kristoffersen, 2012; Mohammadi et al., 2013). The denoising algorithm can be combined with the parameter estimation into one framework to simultaneously reduce the random and physiological noise, which is beyond the scope of this paper.

The current implementation of GL-HOSVD performed the search of similar cuboids on images of all b values. Since the non DW image has higher SNR and contains more structures than DW images, the search of similar cuboids can also be achieved using non DW image only. We tried both approaches on the data in this study, and found they produced similar denoising results.

In terms of computing time, for the simulated DW images with matrix size of 256×256 and 44 diffusion directions, NLM took approximately 1.5 min, LR+Edge 33 min, and GL-HOSVD 14 min on average in our implementation. All methods adopted a single-threaded implementation and were performed in MATLAB 7.12.0 on a Windows 7 computer equipped with an Intel(R) Core(TM)2, 2.33 GHz CPU, and 8 GB RAM. In the proposed method, the global HOSVD stage is much less than 1 min. The local HOSVD stage is the most time consuming part, and can be speeded up by using parallel computation techniques. The implementation of GL-HOSVD¹ (slice-by-slice) and GL-HOSVD² (3D) on the $148 \times 148 \times 90$ volume data with 15 diffusion directions took 40 min and 2.5 h, respectively.

In conclusion, we demonstrate the feasibility of denoising DW MRI data using the HOSVD transform and present a novel GL-HOSVD denoising algorithm. The proposed algorithm employs a global HOSVD stage to guide the conventional patch-based HOSVD denoising method to reduce the visible artifacts in denoised images. The results on simulated and *in vivo* data demonstrate that the proposed algorithm can successfully preserve rapid-changing details in DW images while

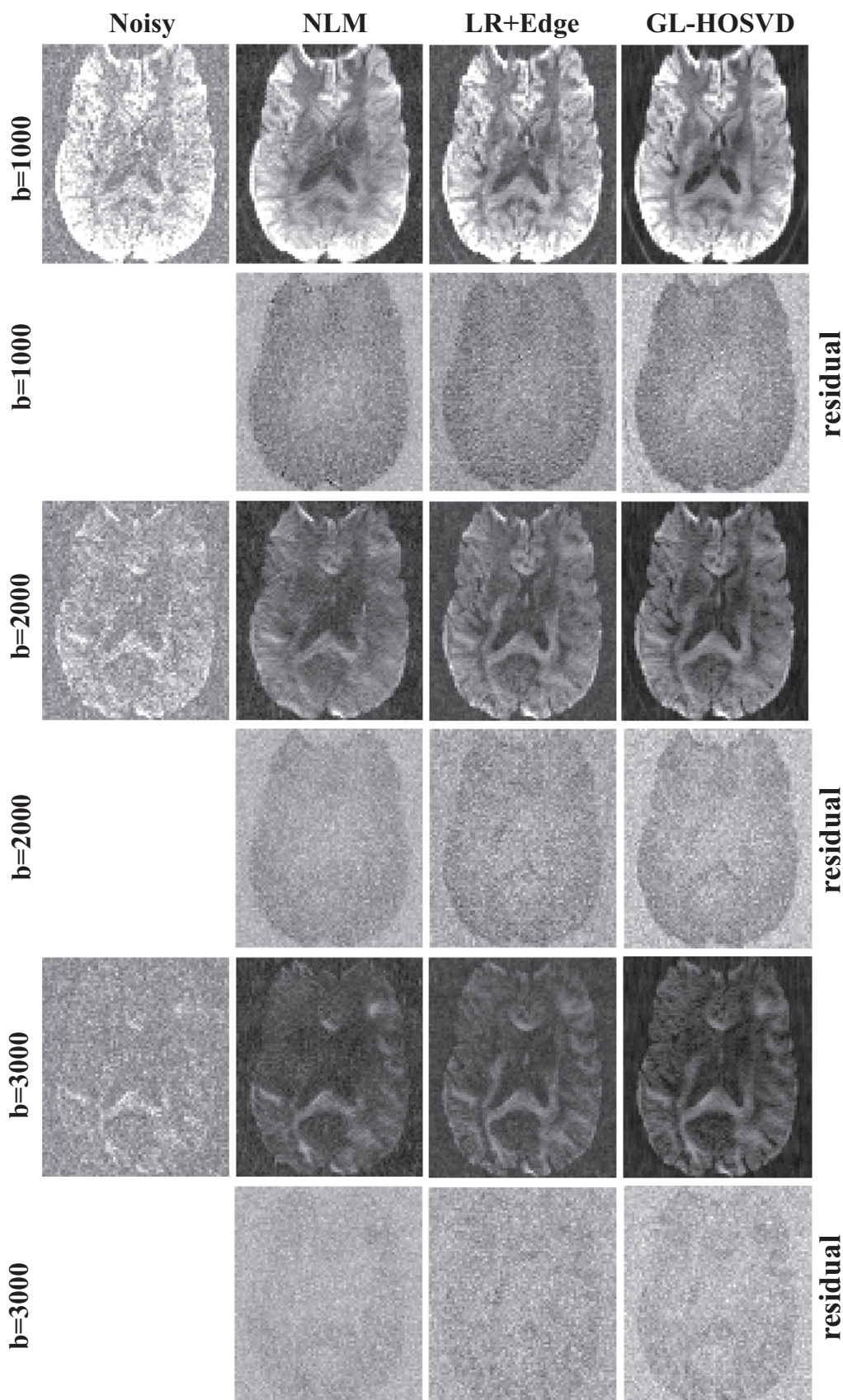


Fig. 12. Comparison of the NLM, LR+Edge and GL-HOSVD algorithms using the first *in vivo* DW data. The multi-b-value DW images along one representative diffusion direction are presented. The residual images show the difference between the noisy and denoised images.

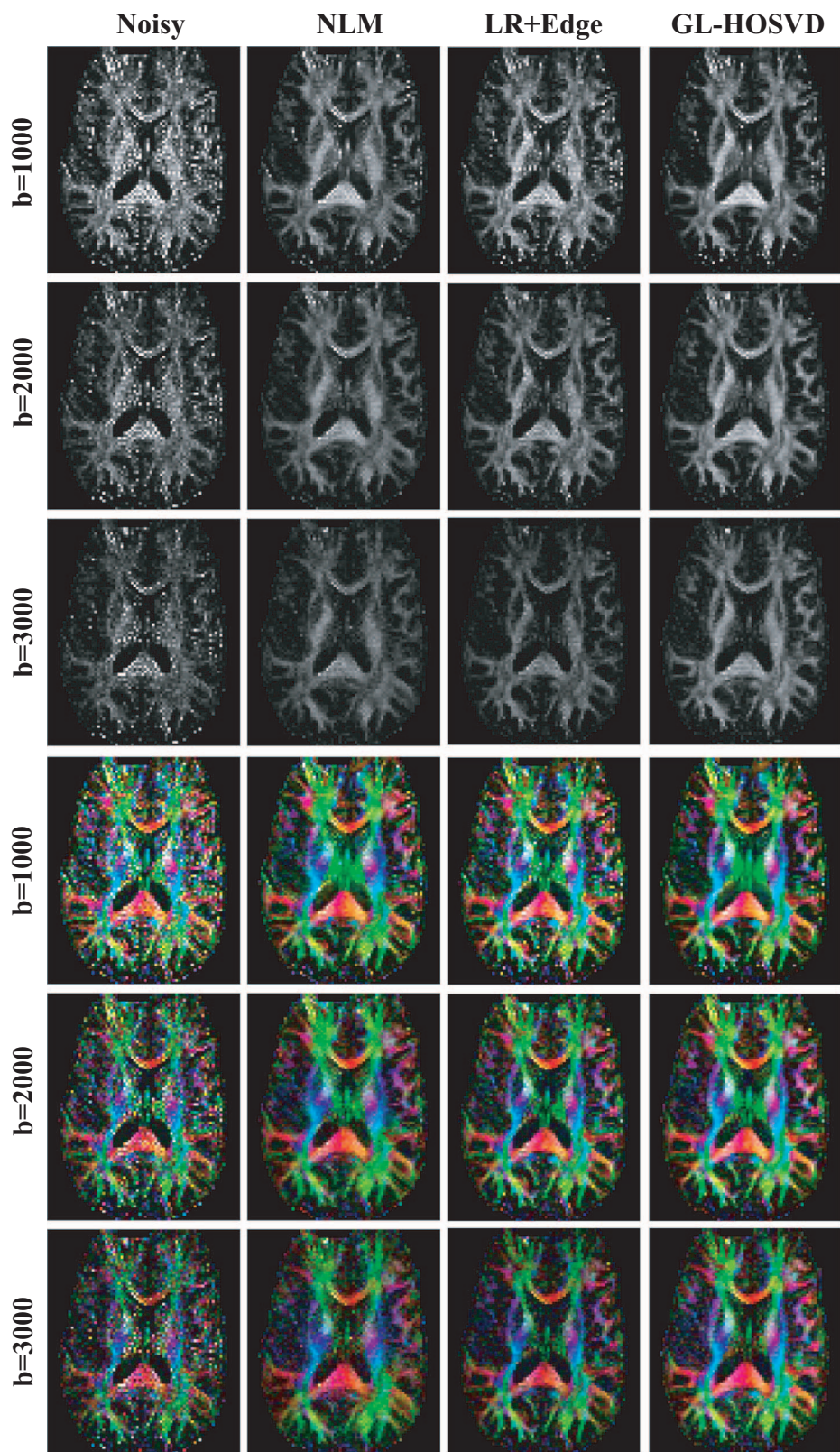


Fig. 13. Comparison of the FA maps (the first three rows) and color-coded FA maps (the last three rows) calculated from the corresponding denoised images in Fig. 12.

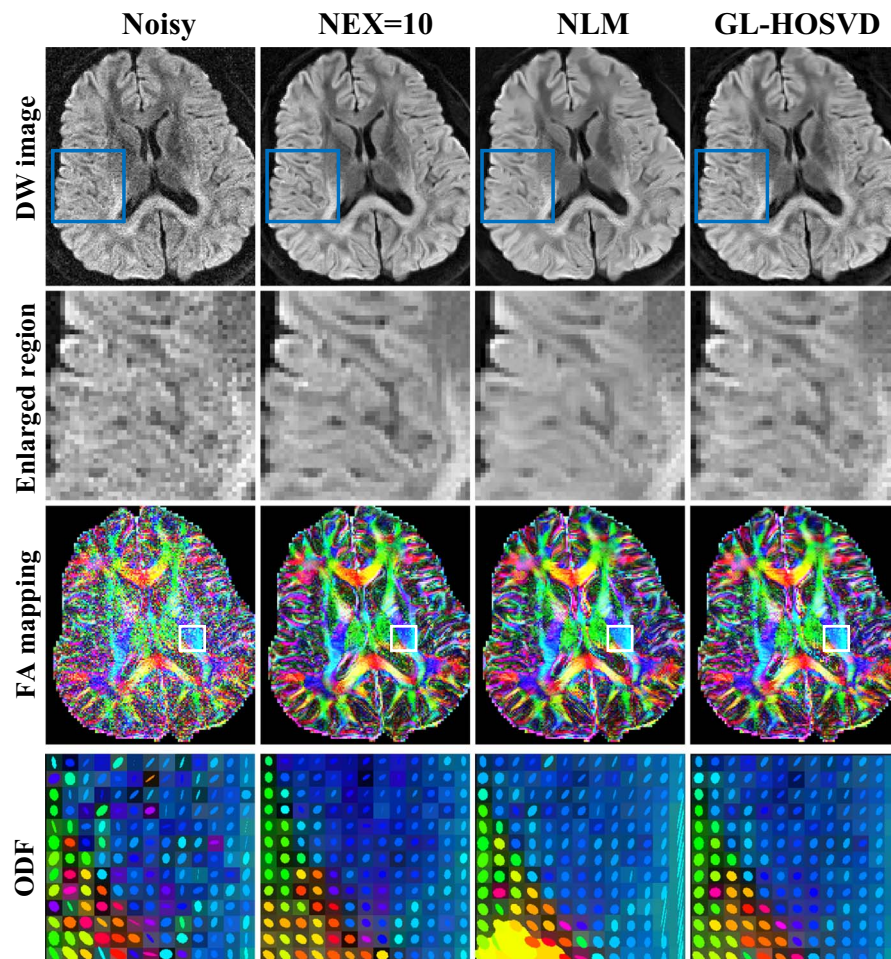


Fig. 14. Denoising results of the second *in vivo* DW data using the NLM and GL-HOSVD algorithms. Top row, from left to right: the noisy image, the reference image acquired using multiple averages (NEX=10), the NLM-filtered image and the GL-HOSVD-filtered image along a representative direction at $b=1000 \text{ s/mm}^2$; Second row: the corresponding enlarged images in the blue square of top row; Third row, the corresponding color-coded FA maps; Bottom row, the corresponding ODFs in the white square of third row.

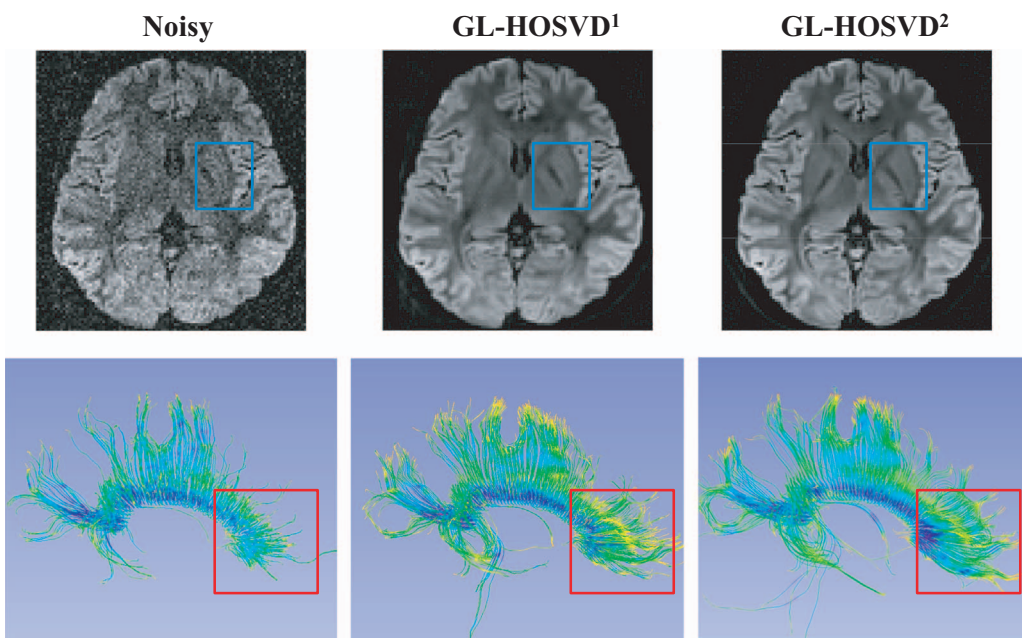


Fig. 15. The application of the GL-HOSVD algorithm to volumetric DW data at $b=1000 \text{ s/mm}^2$ and along multiple diffusion directions. A representative slice along a representative direction is presented. Top row, the noisy image, and the images denoised by two versions of GL-HOSVD (GL-HOSVD¹: slice-by-slice filtering; GL-HOSVD²: 3D filtering). Second row, the corresponding fiber tracking results for the corpus callosum area.

reducing noise and substantially improve the subsequent diffusion parameter quantification. We expect that the proposed method will benefit the application of high-resolution and high b-value DWI in the future.

Acknowledgements

We wish to thank Fan Lam and Zhipei Liang for the source code of their denoising algorithm and constructive discussions. This study was supported by the National Natural Science Foundation of China (81601564, 61671228, 61471187 and U1501256), the China Postdoctoral Science Foundation Projects (2016M602490), the Province Natural Science Fund of Guangdong (2016A030310380), the National Key Technology R & D Program (2015BAI01B03) and a grant from Hong Kong Research Grant Council (RGC C7048-16G). The data used in simulation experiment was acquired through and provided by the Biomedical Informatics Research Network under the following support: U24-RR021760, Mouse Biomedical Informatics Research Network and U24 GM104203, Bio-Informatics Research Network Coordinating Center (BIRN-CC).

References

- Aja-Fernandez, S., Tristan-Vega, A., 2012. Influence of noise correlation in multiple-coil statistical models with sum of squares reconstruction. *Magn. Reson. Med.* 67, 580–585.
- Arfanakis, K., Cordes, D., Haughton, V.M., Carew, J.D., Meyerand, M.E., 2002. Independent component analysis applied to diffusion tensor MRI. *Magn. Reson. Med.* 47, 354–363.
- Bao, L., Robini, M., Liu, W., Zhu, Y., 2013. Structure-adaptive sparse denoising for diffusion-tensor MRI. *Med. Image Anal.* 17, 442–457.
- Bastin, M.E., Armitage, P.A., Marshall, I., 1998. A theoretical study of the effect of experimental noise on the measurement of anisotropy in diffusion imaging. *Magn. Reson. Imaging* 16, 773–785.
- Becker, S.M.A., Tabelow, K., Mohammadi, S., Weiskopf, N., Polzehl, J., 2014. Adaptive smoothing of multi-shell diffusion weighted magnetic resonance data by msPOAS. *NeuroImage* 95, 90–105.
- Becker, S.M.A., Tabelow, K., Voss, H.U., Anwander, A., Heidemann, R.M., Polzehl, J., 2012. Position-orientation adaptive smoothing of diffusion weighted magnetic resonance data (POAS). *Med. Image Anal.* 16, 1142–1155.
- Bernstein, M.A., Thomasson, D.M., Perman, W.H., 1989. Improved detectability in low signal-to-noise ratio magnetic resonance images by means of a phase-corrected real reconstruction. *Med. Phys.* 16, 813–817.
- Bode, M.K., Ruohonen, J., Nieminen, M.T., Pyhtinen, J., 2006. Potential of diffusion imaging in brain tumors: a review. *Acta Radiol.* 47, 585–594.
- Buades, A., Coll, B., Morel, J.M., 2005. A review of image denoising algorithms, with a new one. *Multiscale Model. Simul.* 4, 490–530.
- Castaño-Moraga, C.A., Lenglet, C., Deriche, R., Ruiz-Alzola, J., 2007. A Riemannian approach to anisotropic filtering of tensor fields. *Signal Process.* 87, 263–276.
- Chang, L.C., Walker, L., Pierpaoli, C., 2012. Informed RESTORE: a method for robust estimation of diffusion tensor from low redundancy datasets in the presence of physiological noise artifacts. *Magn. Reson. Med.* 68, 1654–1663.
- Chatterjee, P., Milanfar, P., 2010. Is denoising dead? *IEEE Trans. Image Process.* 19, 895–911.
- Chen, N.K., Guidon, A., Chang, H.C., Song, A.W., 2013. A robust multi-shot scan strategy for high-resolution diffusion weighted MRI enabled by multiplexed sensitivity-encoding (MUSE). *NeuroImage* 72, 41–47.
- Constantinides, C.D., Atalar, E., McVeigh, E.R., 1997. Signal-to-noise measurements in magnitude images from NMR phased arrays. *Magn. Reson. Med.* 38, 852–857.
- Dabov, K., Foi, A., Katkovnik, V., Egiazarian, K., 2007. Image denoising by sparse 3-D transform-domain collaborative filtering. *IEEE Trans. Image Process.* 16, 2080–2095.
- De Lathouwer, L., De Moor, B., Vandewalle, J., 2000. A multilinear singular value decomposition. *SIAM J. Matrix Anal. Appl.* 21, 1253–1278.
- Descoteaux, M., Wiest-Daessle, N., Prima, S., Barillot, C., Deriche, R., 2008. Impact of rician adapted non-local means filtering on HARDI. *Med. Image Comput. Comput. Assist. Interv.* 11, 122–130.
- Dietrich, O., Ray, J.G., Reeder, S.B., Ingrisch, M., Reiser, M.F., Schoenberg, S.O., 2008. Influence of multichannel combination, parallel imaging and other reconstruction techniques on MRI noise characteristics. *Magn. Reson. Imaging* 26, 754–762.
- Ding, Z., Gore, J.C., Anderson, A.W., 2005. Reduction of noise in diffusion tensor images using anisotropic smoothing. *Magn. Reson. Med.* 53, 485–490.
- Dong, W., Shi, G., Li, X., 2013. Nonlocal image restoration with bilateral variance estimation: a low-rank approach. *IEEE Trans. Image Process.* 22, 700–711.
- Donoho, D.L., Johnstone, J.M., 1994. Ideal spatial adaptation by wavelet shrinkage. *Biometrika* 81, 425–455.
- Eriksson, S.H., Rugg-Gunn, F.J., Symms, M.R., Barker, G.J., Duncan, J.S., 2001. Diffusion tensor imaging in patients with epilepsy and malformations of cortical development. *Brain* 124, 617–626.
- Feng, M., Zhang, X., Gao, H., Xu, Y., Lin, B., Liao, J., Chen, W., Feng, Y., 2014. Optimal region-of-interest MRI R2* measurements for the assessment of hepatic iron content in thalassaemia major. *Magn. Reson. Imaging* 32, 647–653.
- Foi, A., 2011. Noise Estimation and Removal in MR Imaging: The Variance-stabilization Approach. ISBI, Chicago, USA, 1809–1814.
- Grinberg, F., Farrer, E., Kaffanke, J., Oros-Peusquens, A.-M., Shah, N.J., 2011. Non-Gaussian diffusion in human brain tissue at high b-factors as examined by a combined diffusion kurtosis and biexponential diffusion tensor analysis. *NeuroImage* 57, 1087–1102.
- Griswold, M.A., Jakob, P.M., Heidemann, R.M., Nittka, M., Jellus, V., Wang, J., Kiefer, B., Haase, A., 2002. Generalized autocalibrating partially parallel acquisitions (GRAPPA). *Magn. Reson. Med.* 47, 1202–1210.
- Halder, J.P., Sakaie, K., Liang, Z., 2009. Resolution and noise properties of linear phase-constrained partial Fourier. In: Proceedings of the 17th Annual Meeting of ISMRM, Honolulu, Hawaii, USA, p. 2862.
- Hamarneh, G., Hradsky, J., 2007. Bilateral filtering of diffusion tensor magnetic resonance images. *IEEE Trans. Image Process.* 16, 2463–2475.
- Henkelman, R.M., 1985. Measurement of signal intensities in the presence of noise in MR images. *Med. Phys.* 12, 232–233, (12, 232–233).
- Hugg, J.W., Butterworth, E.J., Kuzniecky, R.I., 1999. Diffusion mapping applied to mesial temporal lobe epilepsy: preliminary observations. *Neurology* 53, 173–176.
- Jones, D.K., Basser, P.J., 2004. Squashing peanuts and smashing pumpkins: how noise distorts diffusion-weighted MR data. *Magn. Reson. Med.* 52, 979–993.
- Jones, D.K., Simmons, A., Williams, S.C., Horsfield, M.A., 1999. Non-invasive assessment of axonal fiber connectivity in the human brain via diffusion tensor MRI. *Magn. Reson. Med.* 42, 37–41.
- Kloska, S.P., Wintermark, M., Engelhorn, T., Fiebach, J.B., 2010. Acute stroke magnetic resonance imaging: current status and future perspective. *Neuroradiology* 52, 189–201.
- Knaus, C., Zwicker, M., 2013. Dual-domain Image Denoising ICIP.
- Knaus, C., Zwicker, M., 2014. Progressive image denoising. *IEEE Trans Image Process.* 23, 3114–3125.
- Koay, C.G., Ozarslan, E., Basser, P.J., 2009a. A signal transformational framework for breaking the noise floor and its applications in MRI. *J. Magn. Reson.* 197, 108–119.
- Koay, C.G., Ozarslan, E., Pierpaoli, C., 2009b. Probabilistic identification and estimation of noise (PIESNO): a self-consistent approach and its applications in MRI. *J. Magn. Reson.* 199, 94–103.
- Kolda, T.G., Bader, B.W., 2009. Tensor decompositions and applications. *SIAM Rev.* 51, 455–500.
- Krabbe, K., Gideon, P., Wagn, P., Hansen, U., Thomsen, C., Madsen, F., 1997. MR diffusion imaging of human intracranial tumours. *Neuroradiology* 39, 483–489.
- Kristoffersen, A., 2012. Estimating non-gaussian diffusion model parameters in the presence of physiological noise and rician signal bias. *J. Magn. Reson. Imaging* 35, 181–189.
- Lam, F., Babacan, S.D., Halder, J.P., Weiner, M.W., Schuff, N., Liang, Z.-P., 2014. Denoising diffusion-weighted magnitude MR images using rank and edge constraints. *Magn. Reson. Med.* 71, 1272–1284.
- Lam, F., Liu, D., Song, Z., Schuff, N., Liang, Z.-P., 2016. A fast algorithm for denoising magnitude diffusion-weighted images with rank and edge constraints. *Magn. Reson. Med.* 75, 433–440.
- Letexier, D., Bourennane, S., 2008. Adaptive flattening for multidimensional image restoration. *IEEE Signal Process. Lett.* 15, 229–232.
- Levin, A., Nadler, B., 2011. Natural image denoising: optimality and inherent bounds. *Comput. Vision. Pattern Recognit. (CVPR)*, 2833–2840.
- Liu, M., Vemuri, B.C., Deriche, R., 2013. A robust variational approach for simultaneous smoothing and estimation of DTI. *NeuroImage* 67, 33–41.
- Maggioni, M., Katkovnik, V., Egiazarian, K., Foi, A., 2013. Nonlocal transform-domain filter for volumetric data denoising and reconstruction. *IEEE Trans. Image Process.* 22, 119–133.
- Manjón, J.V., Coupé, P., Martí-Bonmatí, L., Collins, D.L., Robles, M., 2010. Adaptive non-local means denoising of MR images with spatially varying noise levels. *J. Magn. Reson. Imaging* 31, 192–203.
- Manjón, J., Carbonellballeiro, J., Lull, J., Garciamartí, G., Martibonmatí, L., Robles, M., 2008. MRI denoising using non-local means. *Med. Image Anal.* 12, 514–523.
- Manjón, J.V., Coupe, P., Buades, A., 2015. MRI noise estimation and denoising using non-local PCA. *Med. Image Anal.* 22, 35–47.
- Manjón, J.V., Coupe, P., Concha, L., Buades, A., Collins, D.L., Robles, M., 2013. Diffusion weighted image denoising using overcomplete local PCA. *PLoS One*, 8.
- Mohammadi, S., Hutton, C., Nagy, Z., Josephs, O., Weiskopf, N., 2013. Retrospective correction of physiological noise in DTI using an extended tensor model and peripheral measurements. *Magn. Reson. Med.* 70, 358–369.
- Pierazzo, N., Lebrun, M., Raisy, M.E., Morel, J.M., Facciolo, G., 2014. Non-Local Dual Image Denoising ICIP.
- Parker, G.J., Schnabel, J.A., Symms, M.R., Werring, D.J., Barker, G.J., 2000. Nonlinear smoothing for reduction of systematic and random errors in diffusion tensor imaging. *J. Magn. Reson. Imaging* 11, 702–710.
- Poupon, C., Mangin, J., Clark, C.A., Frouin, V., Regis, J., Le Bihan, D., Bloch, I., 2001. Towards inference of human brain connectivity from MR diffusion tensor data. *Med. Image Anal.* 5, 1–15.
- Pruessmann, K.P., Weiger, M., Scheidegger, M.B., Boesiger, P., 1999. SENSE: sensitivity encoding for fast MRI. *Magn. Reson. Med.* 42, 952–962.
- Rajwade, A., Rangarajan, A., Banerjee, A., 2013. Image denoising using the higher order singular value decomposition. *IEEE Trans. Pattern Anal. Mach. Intell.* 35, 849–862.
- Shimamoto, H., Oshio, K., Tanimoto, A., Higuchi, N., Okuda, S., Kurabayashi, S., Mulkern, R.V., 2009. Biexponential apparent diffusion coefficients in prostate cancer. *Magn. Reson. Imaging* 27, 355–359.

- Sotak, C.H., 2002. The role of diffusion tensor imaging in the evaluation of ischemic brain injury – a review. *NMR Biomed.* 15, 561–569.
- Stein, 1981. Estimation of the mean of a multivariate normal distribution. *Ann. Stat.*, 9, Tievsky, A.L., Ptak, T., Farkas, J., 1999. Investigation of apparent diffusion coefficient and diffusion tensor anisotropy in acute and chronic multiple sclerosis lesions. *AJNR Am. J. Neuroradiol.* 20, 1491–1499.
- Tschumperlé, D., Deriche, R., 2003. Variational frameworks for DT-MRI estimation, regularization and visualization. In: Proceedings of the Ninth IEEE International Conference on Computer Vision, 2003, pp. 116–121.
- Ügurbil, K., Xu, J., Auerbach, E.J., Moeller, S., Vu, A.T., Duarte-Carvalhalino, J.M., Lenglet, C., Wu, X., Schmitter, S., Van de Moortele, P.F., Strupp, J., Sapiro, G., De Martino, F., Wang, D., Harel, N., Garwood, M., Chen, L., Feinberg, D.A., Smith, S.M., Miller, K.L., Sotiropoulos, S.N., Jbabdi, S., Andersson, J.L.R., Behrens, T.E.J., Glasser, M.F., Van Essen, D.C., Yacoub, E., 2013. Pushing spatial and temporal resolution for functional and diffusion MRI in the human connectome project. *NeuroImage* 80, 80–104.
- Veraart, J., Fieremans, E., Novikov, D.S., 2015. Diffusion MRI noise mapping using random matrix theory. *Magn. Reson. Med.*
- Wang, Z., Vemuri, B.C., Chen, Y., Mareci, T., 2003. A constrained variational principle for direct estimation and smoothing of the diffusion tensor field from DWI. *Inf. Process. Med. Imaging* 18, 660–671.
- Wang, Z., Vemuri, B.C., Chen, Y., Mareci, T.H., 2004. A constrained variational principle for direct estimation and smoothing of the diffusion tensor field from complex DWI. *IEEE Trans. Med. Imaging* 23, 930–939.
- Werring, D.J., Clark, C.A., Barker, G.J., Thompson, A.J., Miller, D.H., 1999. Diffusion tensor imaging of lesions and normal-appearing white matter in multiple sclerosis. *Neurology* 52, 1626–1632.
- Wiest-Daessle, N., Prima, S., Coupe, P., Morrissey, S.P., Barillot, C., 2007. Non-local means variants for denoising of diffusion-weighted and diffusion tensor MRI. *Med. Image Comput. Comput. Assist. Interv.* 10, 344–351.
- Wirestam, R., Bibic, A., Lätt, J., Brockstedt, S., Ståhlberg, F., 2006. Denoising of complex MRI data by wavelet-domain filtering: application to high-b-value diffusion-weighted imaging. *Magn. Reson. Med.* 56, 1114–1120.
- Wu, E.X., Cheung, M.M., 2010. MR diffusion kurtosis imaging for neural tissue characterization. *NMR Biomed.* 23, 836–848.
- Yu, Y.Y., Jin, J., Liu, F., Crozier, S., 2014. Multidimensional compressed sensing MRI using tensor decomposition-based sparsifying transform. *PLoS One*, 9.
- Zhang, X., Xu, Z., Jia, N., Yang, W., Feng, Q., Chen, W., Feng, Y., 2015a. Denoising of 3D magnetic resonance images by using higher-order singular value decomposition. *Med. Image Anal.* 19, 75–86.
- Zhang, Z., Huang, F., Ma, X., Xie, S., Guo, H., 2015b. Self-feeding MUSE: a robust method for high resolution diffusion imaging using interleaved EPI. *NeuroImage* 105, 552–560.
- Zhu, X., Milanfar, P., 2010. Automatic parameter selection for denoising algorithms using a no-reference measure of image content. *IEEE Trans. Image Process.* 19, 3116–3132.